EVOLUTIONARY BIOLOGY

Reconstruction of distinct vertebrate gastrulation modes via modulation of key cell behaviors in the chick embryo

Manli Chuai[1]†, Guillermo Serrano Nájera[1]*†‡, Mattia Serra[2], Lakshminarayanan Mahadevan[3,4], Cornelis J. Weijer[1]*

The morphology of gastrulation driving the internalization of the mesoderm and endoderm differs markedly among vertebrate species. It ranges from involution of epithelial sheets of cells through a circular blastopore in amphibians to ingression of mesenchymal cells through a primitive streak in amniotes. By targeting signaling pathways controlling critical cell behaviors in the chick embryo, we generated crescent- and ring-shaped mesendoderm territories in which cells can or cannot ingress. These alterations subvert the formation of the chick primitive streak into the gastrulation modes seen in amphibians, reptiles, and teleost fish. Our experimental manipulations are supported by a theoretical framework linking cellular behaviors to self-organized multicellular flows outlined in detail in the accompanying paper. Together, this suggests that the evolution of gastrulation movements is largely determined by changes in a few critical cell behaviors in the mesendoderm territory across different species and controlled by a relatively small number of signaling pathways.

INTRODUCTION

During gastrulation, embryos transform from a simple epithelial layer into a three-layer structure. In vertebrate embryos, this process requires large morphogenetic movements that locate the three primary germ layers—the ectoderm, mesoderm, and endoderm—in their topologically correct positions (*1*, *2*). However, the detailed tissue movements and morphology of the embryo during gastrulation vary greatly among vertebrate animals (*3*). For example, *Xenopus* forms a blastopore through which the mesoderm and endoderm precursors internalize as epithelial sheets, while, at the other end of the spectrum, amniote embryos such as chick, mouse, and human embryos internalize these precursors as mesenchymal cells through a structure known as the primitive streak (*4*, *5*).

The morphogenetic tissue flows in all organisms result from the integration of a few critical cell behaviors, including cell division, differentiation, shape changes, and movement. These cell behaviors are patterned and coordinated through a combination of short- and long-range chemical and mechanical signals (*6*–*8*). Different spatiotemporal organizations of these cell behaviors, in conjunction with geometrical and mechanical constraints imposed by the size and shape of the embryo and extraembryonic tissues, are thought to determine the diverse morphogenetic programs in vertebrate gastrulation (*9*, *10*). However, how the large-scale cell movements are coordinated and coupled via feedback to the signaling processes as part of robust developmental control mechanisms remains to be resolved (*11*–*14*).

The formation of the primitive streak in the chick embryo involves intercalation of cells in the sickle-shaped mesendoderm precursor domain initially located in the posterior epiblast of the embryo followed by ingression of these cells in the primitive streak (*15*, *16*). Previously, we established quantitative light sheet microscopy and computational data analysis methods to characterize both the embryo-wide tissue flows and critical cell behaviors driving them during streak formation (*15*). This showed quantitatively how the tissue flows underlying streak formation are driven by directional cell intercalations and ingression of the mesendoderm precursor cells. Furthermore, the directional cell intercalations were shown to be associated with and dependent on myosin cables in cellular junctions aligned in the direction of intercalation (*15*). We here confirm and expand these findings and undertake a study to investigate how the modulation of a limited number of critical cell behaviors during gastrulation in the chick embryo alters the spatiotemporal dynamics and morphology of gastrulation.

RESULTS

Using the chick embryo as a model organism, we explore how the patterning of cell behaviors determines primitive streak morphogenesis during gastrulation (Fig. 1, A to C and G). To study the tissue-wide coordination of the cell behaviors in the epiblast, we image, as before, gastrulation in a chick line expressing a membrane-targeted green fluorescent protein (GFP) using a custom-built light sheet microscope (*15*) and image analysis (see Materials and Methods and movie S1).

Quantitation of cell flows and behaviors

The dynamics of tissue deformation (Fig. 1D) can be directly quantified by measuring changes in the velocity field associated with tissue shape changes and movement using particle image

[1]Division of Cell and Developmental Biology, School of Life Sciences, University of Dundee, Dundee DD1 5EH, UK. [2]Department of Physics, University of California San Diego, La Jolla, CA 92093, USA. [3]School of Engineering and Applied Sciences, Harvard University, Cambridge, MA 02134, USA. [4]Departments of Physics and Organismic and Evolutionary Biology, Harvard University, Cambridge, MA 02138, USA.
*Corresponding author. Email: gs714@cam.ac.uk (G.S.N.); c.j.weijer@dundee.ac.uk (C.J.W.)
†These authors contributed equally to this work.
‡Present address: Department of Genetics, University of Cambridge, Cambridge CB2 3EH, UK.

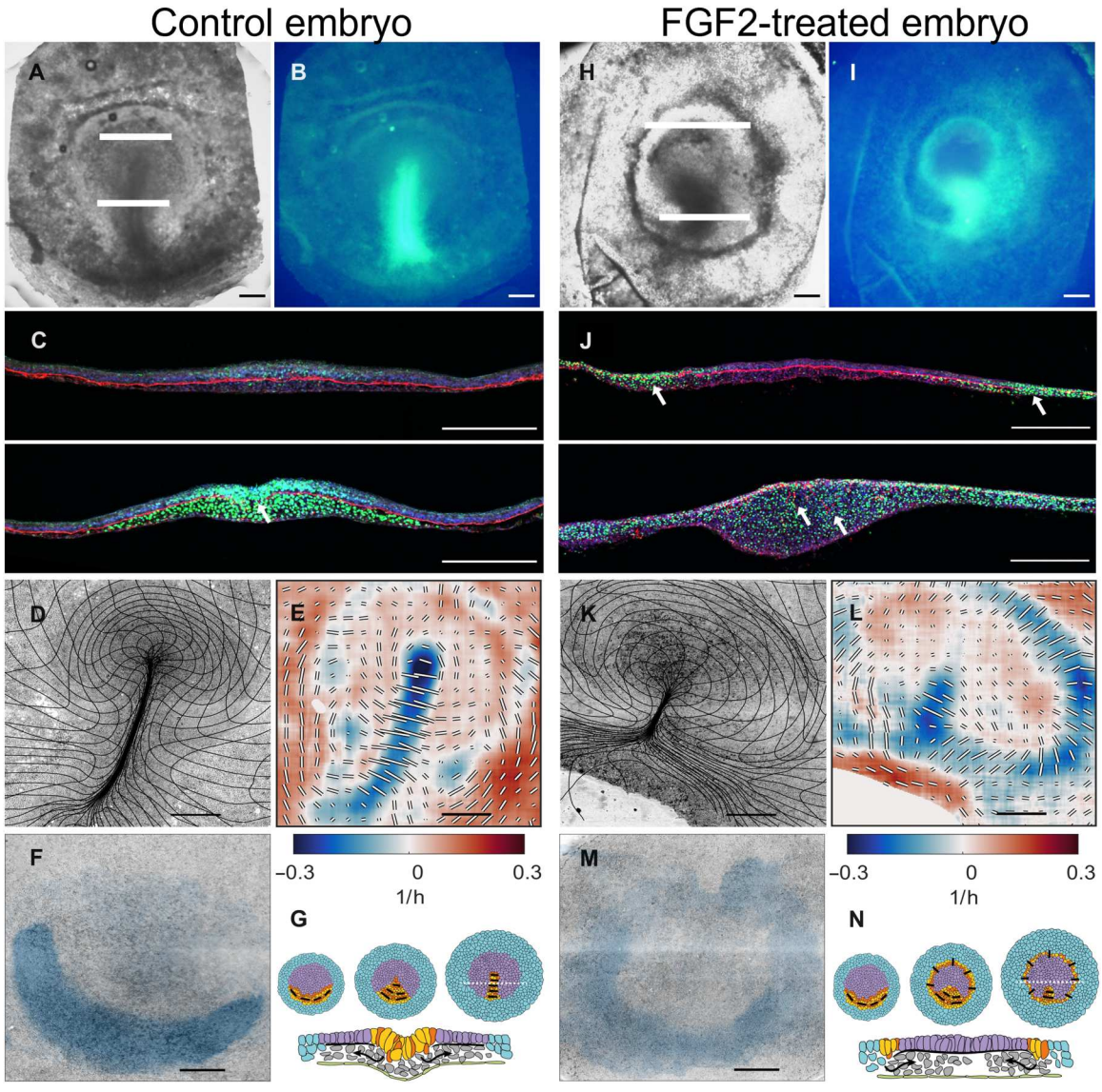

Fig. 1. Characterization of gastrulation for control embryo and after FGF2 treatment. (**A**) Control, bright-field image of embryo at HH3$^+$. (**B**) SNAI expression in embryo shown in (A). (**C**) Two sections taken at the white lines in (A) showing SNAI (green), FN1 (red), and actin (blue). Note that in the streak, the FN1 layer is fragmented as indicated by the white arrow. (**D**) Overview images of embryo from light sheet microscope at the end (HH3$^+$) of the experiment overlaid with a deformation mesh. (**E**) Strain rate tensor for stages shown in (D). Isotropic strain rate component shown as color blue for contraction and red for expansion. The anisotropic part of the strain rate tensor is shown as black and white bars indicating the magnitude and direction of contraction. (**F**) Cells that will ingress through the streak [domain of attraction (DOA)] during the experiment calculated from the dynamic morphoskeleton (DM). (**G**) Schematic summary of development (stages HH1, HH2, and HH3), extraembryonic area in blue, mesendoderm precursors in yellow/red, and embryonic area in purple; black bars show the direction of cell intercalation, section taken at the broken white line in HH3 embryo schematic in (E). Scale bars, 500 μm except in (C), which is 250 μm. For (E) and (L), the anisotropic scale bar length represents 0.5/hour for the anisotropic component of the strain rate. (**H** to **N**) Same layout as (A) to (F) for FGF2-treated embryo for the same time as the control embryo. FGF (50 μg/ml on the hypoblast; see Materials and Methods)–treated embryos generate a circular primitive streak surrounding the epiblast (eight of eight treated embryos in the light sheet microscope).

velocimetry (PIV; fig. S1, A and B). We previously showed that the decomposed strain rates calculated from the velocity fields are a robust indicator of individual cell behaviors driving the tissue flows and allow the identification and quantification of cell behaviors resulting from different perturbations (*15*, *17*). Negative values of the isotropic part of the strain rate, associated with a decrease in tissue area, denote regions where cells are undergoing apical contraction and cell ingression. Areas characterized by larger values in the anisotropic components of the strain rate, associated with shear deformation, indicate the convergence and extension of the tissue produced by directed cell intercalations (fig. S2 and movie S2). Our current observations on whole embryos confirm our earlier observations on embryo slices (*15*) that the primitive streak forms in a region undergoing convergent extension produced by apical contraction and cell ingression (negative values of the isotropic strain rate tensor) and cell intercalation (contracting anisotropic component of the strain rate tensor oriented perpendicular to the streak) (Fig. 1E).

Quantifying the scale and nature of these movements requires an effective description of the relative motions of cells. While Eulerian quantities (decomposed strain rates) correlate with distinct cell behaviors, morphogenetic features arise from different processes integrated over space and time along cell trajectories. To account for this, we compute the dynamic morphoskeleton (DM) (*18*), which consists of Lagrangian attractors, their domain of attraction (DOA), and repellers that together organize tissue flows [figure 2 and movie 3 of the accompanying paper (*19*)]. The DOA consists of the back projection of the attractor on the initial stage of development and reveals the extent of the sickle-shaped posterior-located mesendoderm precursors fated to ingress through the streak (Fig. 1F). See Materials and Methods for details on DM computation.

Tissue flows are driven by mesoderm cells

Previous work has established how cells in the sickle-shaped posterior territory form the primitive streak. Initially, cell-cell signaling between cells in the extra- and embryonic areas results in the induction of mesendoderm precursors in a sickle-shaped domain in the posterior embryonic epiblast (*20*). These cells then start a myosin II–mediated directional cell-cell intercalation process that drives the convergence and extension of the sickle-shaped mesendoderm in the extending primitive streak (*15*, *21*, *22*). This developmental phase is characterized by large counterrotating vortical flows in the epiblast (fig. S1B), known as polonaise movements (*23*, *24*). During this process, the mesendodermal precursor cells begin to contract apically in preparation for their ingression in the streak (*16*, *25*). Following an epithelial-to-mesenchymal transition (EMT) and ingression, the cells migrate away as cohorts of loosely associated cells (*26*, *27*) to form the various endodermal and mesodermal structures in the embryo (Fig. 1C) (*28*–*30*).

These findings suggest that directed cell intercalation and cell ingression in the mesendoderm territory drive the morphogenetic flows during avian gastrulation. To test this idea, we inhibited mesoderm differentiation by blocking fibroblast growth factor (FGF) signaling using the pan-FGF receptor inhibitor LY2874455 (*31*). The addition of LY2874455 resulted in the complete inhibition of mesoderm differentiation and the loss of the characteristic tissue flows associated with streak formation (movie S3). Analysis of the strain rate shows that there is little organized intercalation, confirming that the presence of mesendoderm tissue is a prerequisite for streak formation (fig. S3).

Mesoderm expansion produces a circular streak

While inhibiting FGF signaling blocks the mesoderm differentiation, the addition of an excess of FGF results in the circular expansion of the SNAI2 (*snail family transcriptional repressor 2*) expression territory along the marginal zone (Fig. 1, H to J), confirming previous observations that *SNAI2*, *brachyury*, and *cChordin* expression is activated by FGF (*20*). During normal development of SNAI2$^+$, mesendoderm cells travel from the sickle-shaped territory where they are specified toward the primitive streak, where they undergo EMT and cell ingression (*25*, *32*). This can be seen via the presence of SNAI2-expressing cells in the inner layers and the breakdown of the Fibronectin 1 (FN1) layer in the streak (Fig. 1, B and C, arrow). Embryos treated with excess FGF show that SNAI2$^+$ cells have extended along a ring-shaped region along the marginal zone (Fig. 1, H to J), while the FN1 basal layer is degraded (Fig. 1J, arrows). In vivo imaging shows that FGF-treated embryos exhibit a ring of tissue (movie S4) that presents the two characteristic signatures of the late primitive streak, isotropic contraction along the ring, indicating that cells in the ring are undergoing apical contraction and ingression. Furthermore, shear contraction across the ring shows that cells intercalate in a direction perpendicular to the circular streak (Fig. 1, K to M, and movie S5). These directional intercalations generate convergent-extending flows along the ring (fig. S4).

The resulting circular streak structure resembles the germ ring of teleost fish gastrulation, where cells undergo ingression and migrate toward the animal pole (*33*–*36*) [see also figure 3F and movie 9 of (*19*) for the corresponding DM]. Similarly, in FGF-treated embryos, cells that ingress in the circular streak migrate toward the center of the epiblast, the corresponding animal pole (movie S6).

Blocking ingression results in epiblast folding

Bone morphogenetic protein (BMP) signaling has been shown to occur in the anterior epiblast before the onset of gastrulation (*37*–*39*). Furthermore, blocking BMP signaling can result in the induction of mesoderm and the generation of ectopic primitive streaks (*37*, *38*, *40*). In line with these previous observations, we induced the expansion of the mesendoderm territory along the anterior marginal zone by blocking BMP signaling using the pan BMP type I receptor (ALK1, ALK2, ALK3, ALK6) inhibitor LDN-193189 (*41*) (LDN; fig. S5, A to D), as seen by the expression of SNAI2$^+$ cells in a circular domain (fig. S5, A to D). Therefore, blocking BMP signaling is an alternative to FGF activation to generate SNAI2-expressing mesendoderm rings. The SNAI2-positive ectopic domains induced by LDN form rapidly and are more circular than those formed after FGF addition, suggesting that relieving inhibition of mesoderm differentiation by LDN acts faster than the induction of mesendoderm by FGF. Blocking Nodal receptors ALK4, ALK5 by the inhibitor SB50124 does not block mesoderm formation (fig. S6). In LDN-treated embryos, concomitant with the formation of the mesoderm ring, we note the appearance of a circular fold at the boundary of the domain, which contracted over time, engulfing the internal epiblast (fig. S5, A to F). The observed tissue buckling after blocking BMP signaling results from the inhibition of EMT and cell ingression, even in the presence of exogenous FGF (figs. S5, G to I, and S7). Closer inspection of the development of these LDN-treated embryos showed that they are noticeably smaller due to substantial inhibition of cell proliferation (fig. S8A). This prevented longer-term observation of the embryos in the light sheet microscope to follow the details of the closure of the ingression rings, because, in the absence of tissue growth but in the presence of extensive tissue buckling and involution, the embryo shrinks and detaches from the vitelline membrane, which is fixed in the light sheet imaging chamber (*42*).

We observed that the combination of the BMP signaling inhibitor LDN and the glycogen synthase kinase 3 (GSK3) inhibitor CHIR-99021 (CHIR), conditions that have been used to produce self-renewing mesendoderm precursors in vitro from induced pluripotent stem and embryonic stem cells (*43*), successfully overcame the LDN-induced shrinking and detachment. Treated embryos still showed the formation of mesodermal precursor rings and inhibition of EMT, resulting in buckling and involution of the central tissue (Fig. 2, A to G, and movie S7), but without significant inhibition of cell division (fig. S8B). Sectioning revealed that tissue in

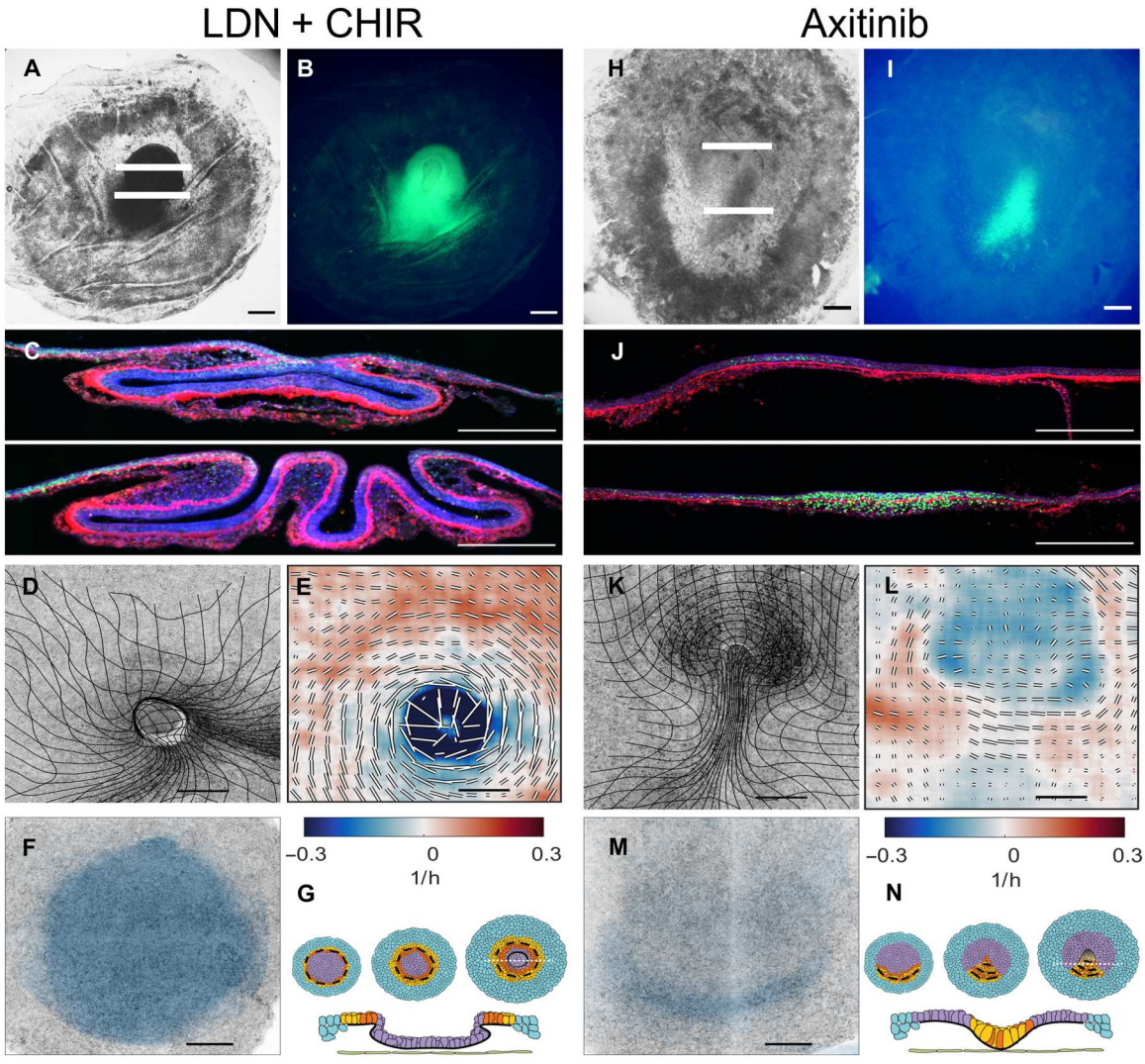

Fig. 2. Characterization of gastrulation in embryos after perturbation of the BMP/Wnt and Vegf signalling pathways. (**A**) Bright-field image of embryo treated with the BMP receptor inhibitor LDN (100 nM) and the GSK3 inhibitor CHIR (3 μM) for 16 hrs from stage HH1 onward (time after which control embryos reach stage HH3$^+$). The embryos generate a large circular invagination that engulfs the central epiblast. (**B**) SNAI2 expression in the embryo shown in (A). (**C**) Two sections taken at the white lines in (A) showing SNAI (green), FN1 (red), and actin (blue). Note that the FN1 layer is not fragmented at the site of invagination. (**D**) Lightsheet microscope overview image of an embryo at the end of the experiment overlaid with a deformation mesh (typical for four of five embryos in the light sheet microscope). (**E**) Strain rate tensor for the embryo shown in (D). Isotropic strain rate component shown as color blue for contraction and red for expansion. The anisotropic part of the strain rate tensor is shown as black and white bars indicating the magnitude and direction of contraction. (**F**) Cells that will ingress through the streak [domain of attraction (DOA)] during the experiment calculated from the dynamic morphoskeleton (DM). (**G**) Schematic of the development of a contractile ring which in the absence of EMT results in the invagination of the central epiblast. (**H** to **N**) Same layout as (A) to (F) for embryos treated for 16 hrs with the vascular endothelial growth factor (VEGF) receptor inhibitor axitinib (100 nM). (H) Bright field image of axinitib treated embryo. (I) SNAI2 expression in embryo shown in (H). Axinitib treated embryos show limited breakdown of FN1 in the posterior streak (J), an inhibition of the isotropic contraction in the region of the primitive streak (L), a pronounced folding in the anterior streak (K) and a reduced ingression of mesendoderm cells in the streak (M) (four of five in the light sheet microscope). (N) Schematic of the formation of the primitive streak, which in the absence of EMT buckles into the embryo.

this internal domain had folded inside the embryo, and the mesendoderm cells that internalized through the circular fold failed to undergo EMT, as shown by the cells staying connected in a continuous epithelial sheet and the presence of a continuous nondegraded layer of FN1 underlying the involuted epithelial cells (Fig. 2G).

Analysis of the anisotropic strain rate (Fig. 2E) in these embryos showed a pronounced contraction oriented tangentially to the ectopic mesendoderm ring produced by cell intercalation (movie S8). The tangential intercalation drives the contraction of the ring, and because these cells do not undergo EMT (Fig. 2C) supported by the absence of apical contraction (movie S8), this contraction does not result in ingression but instead in buckling. The measured negative isotropic strain rate at these stages of buckling indicates the disappearance of cells into the inside of the embryo rather than ingression. This situation reproduces some aspects of the tissue organization and flow during the closing blastopore in

Xenopus, where tissue is invaginated as a continuous epithelial sheet (*44*) [see also figure 3H and movie 12 of (*19*) for the corresponding DM]. However, while *Xenopus* embryos invaginate their vegetal side during gastrulation, in LDN-treated chick embryos, the system resolves to engulf the central epiblast, corresponding to the animal side. This is most likely caused by the attachment of the extraembryonic edge of the embryo to the vitelline membrane functioning as an important mechanical constraint that prevents the invagination of the vegetal side (see also HNF3B expression in the next section).

Last, we explored the effects of blocking growth factors that have been implicated in EMT and the migration of mesoderm cells of the platelet-derived growth factor and vascular endothelial growth factor (VEGF) families (*45*, *46*). Cells in the posterior portion of the primitive streak express VEGFR2 and manifest a chemotactic response to several VEGF isoforms after ingression. We observed that the use of the VEGF signaling inhibitor axitinib (Fig. 2, H to N, and movie S9) (*47*) or competitive VEGFR2-Fc fragments (fig. S9) results in the formation of a short fat streak when added at early stages (2 to 3 hours of incubation). Light sheet microscopy of developing embryos showed that cell intercalation was not significantly inhibited (Fig. 2L), and the vortical flow of tissue into the ventral midline of the embryo continued (movie S10). However, there was a distinct absence of ingression of cells in the streak evidenced by the absence of tissue contraction in the midline (Fig. 2L and fig. S9, A and B) and reduction of FN1 degradation (Fig. 3, axitinib).

The lack of cell ingression at the primitive streak in combination with an unaltered rate of cell division (fig. S9, C and D) results in more cells flowing into the midline than flowing out of it. When the epiblast cannot accommodate more tissue, the anterior portion of the streak can buckle inside (movie S11). Furthermore, the rate of cell proliferation is not affected by blocking VEGF signaling (fig. S9, C and D), suggesting that the buckling is not the result of reduced tissue fluidity produced by a reduced number of dividing cells (*48*). The resulting fold structure might resemble the blastoporal canal observed in chameleon gastrulation (*49*) [see also figure 3D and movie 7 of (*19*) for the corresponding DM]. Chameleon gastrulation is bimodal, they internalize part of the anterior mesoderm by involution through the blastoporal canal, and the posterior mesoderm is internalized by a limited amount by individual cell ingressions through the blastoporal plate (*50*). Intriguingly, the reduction of the individual cell ingression in the primitive streak of the chick embryo can originate a similar anterior invagination.

Mode of ingression and cell type identities after perturbation

The breakdown of the basement membrane is necessary for EMT to occur and cells to ingress through the primitive streak (*5*, *25*, *51*). To further characterize the mode of ingression associated with each chemical perturbation, we analyzed the breakdown of the basement membrane by inspecting the meshwork of FN1 (Fig. 3) and tenascin C (TNC; fig. S10) (*25*, *52*, *53*). During normal development, the anterior epiblast shows a very dense FN1 layer (Fig. 3, control). The region of SNAI2 expression in the primitive streak, where cells undergo EMT and ingress, is associated with the formation of large pores in the FN1 network (Fig. 3, control), as has been observed in mice (*54*). Furthermore, this region is characterized by the assembly of oriented fibers of TNC (fig. S10, control). This situation is fully reproduced in the ectopic ring of SNAI2 expression generated in FGF2-treated embryos (Fig. 3, FGF2, and fig. S10, FGF2), further supporting the idea that this ring functions as a circular primitive streak (Fig. 1, H to N).

Instead, the ectopic ring of SNAI2 expression generated in LDN-treated embryos is not associated with large pores in the FN1 network (Fig. 3, LDN + CHIR) or the TNC fiber assembly (fig. S10, LDN), suggesting that cell ingression associated with EMT is blocked in LDN-treated embryos. Combined LDN and FGF treatment, which results in the formation of a large invagination, indicating that LDN dominates at the morphogenetical level (fig. S5, G to K), shows FN1 breakdown (fig. S5I, arrow) and assembly of TNC fibers (fig. S10, FGF2 + LDN), indicating that there could be a partial EMT and possibly some cell ingression. Last, axitinib-treated embryos show a less defined FN1 meshwork along the primitive streak (Fig. 3, axitinib), associated with a reduction of cell ingression.

In addition, we studied whether the ectopic rings of $SNAI2^+$ cells generated with different treatments have a more endodermal or mesodermal character. The tip of the primitive streak is a source of endoderm precursors, and it is characterized by the expression of the transcription factor HNF3B, a marker of the definitive endoderm (*55*–*57*). We noted that cells in the tip of the streak showed reduced levels of SNAI2 expression concomitant with elevated HNF3B expression (figs. S11 and S12, control). It is noteworthy that scattered HNF3B-expressing cells are also found in the epiblast anterior to the streak (fig. S12, control). Among the ectopic ring of SNAI2-expressing cells in FGF-treated embryos, some scattered $HNF3B^+$ cells can also be observed; however, their expression levels and density are not the same as in the tip of the streak remnants, suggesting that FGF treatment especially induces mesoderm precursors (fig. S12, FGF). In LDN-treated embryos, a large population of the SNAI2-expressing cells in the ring coexpresses HNF3B (fig. S12, LDN), which might indicate that these cells are shifted toward an endoderm precursor fate. Furthermore, LDN-treated embryos show elevated HNF3B expression across the central epiblast (fig. S12, LDN), which will be engulfed by the contracting ring. Intriguingly, this makes this process more similar to *Xenopus* gastrulation, where the endoderm is also engulfed by the contracting blastopore.

Aligned myosin cables direct intercalations

Our experiments show that the shape of the mesendoderm, together with cell intercalation and ingression behaviors, determines the morphogenetic outcome of gastrulation. While cell intercalations drive the main in-plane tissue flows, the presence or absence of individual cell ingressions determines whether the tissue will remain flat or will buckle. During normal development, the direction of intercalations of mesendoderm cells is strongly correlated with the direction of cables of phosphorylated myosin II that span several cells (*15*). At early gastrulation stages, these myosin cables extend from posterior to anterior, creating a semicircle between the embryonic and extraembryonic territories, and they correlate with the direction of intercalation, as shown by the intercalation (P) tensor (*58*) computed from cell tracking data (Fig. 4A), as described in detail in our previous work (*15*). We show that this strong correlation between mesendoderm expression domain and myosin planar cell polarity persists in the cases of circular mesendoderm domains, as verified with the FGF2 and LDN treatments (Fig. 4, B and C). As in normal early development, the myosin planar cell polarity is initially

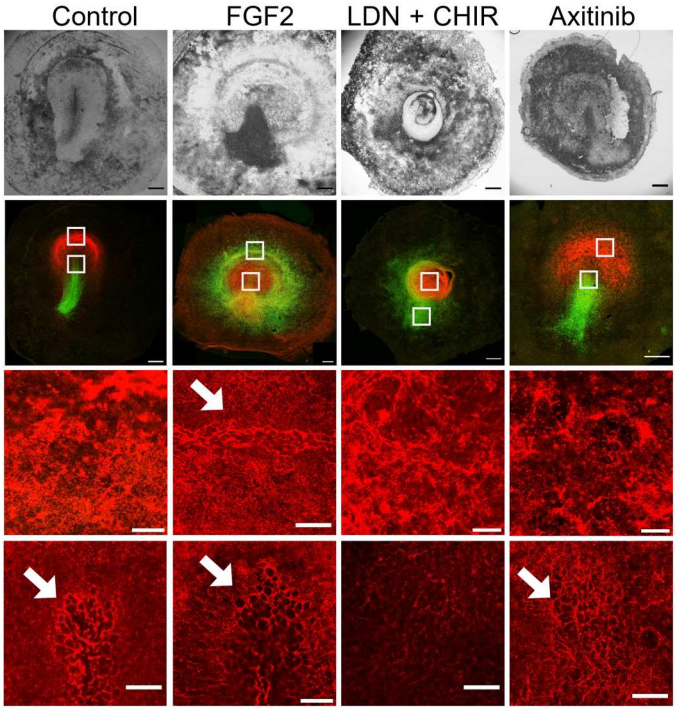

Fig. 3. Comparison of SNAI and FN1 expression after various perturbations. Top row: Bright-field images of embryos after 16 hours in EC culture after various treatments. Second row: Confocal images of the embryos in the top row showing the expression of SNAI (green) and FN1 (red). Third and fourth rows: Higher-magnification images taken in front of the streak (top white square) and at the tip of the streak (bottom white square). It can be seen in the control (first row) that the region anterior to the streak expresses high levels of FN1, forming a densely packed meshwork of fibrils. In the streak, FN1 shows a larger pore meshwork (arrows) probably associated with cell ingressions. Note that in the ring-shaped streak after FGF treatment (second column), FN1 shows the same large porous structure as in the streak, indicating that this is also a region where the cells ingress. After LDN and axitinib treatment, the anterior region shows a dense fibrillar network, while in the streak or ring cases, the porous network is less well developed as in the control or after FGF treatment. The data show that the presence or absence of ingression is reflected in the FN1 network structure. Scale bars, 500 μm (two top rows) and 100 μm (two bottom rows).

oriented along the long axis of the mesendoderm expression domain, in the same direction of cell intercalations, which explains the contraction of the ring in the LDN + CHIR case. However, during normal streak extension at late stages (HH3 to HH4), cell intercalations orient perpendicular to the long axis of the mesendoderm (the primitive streak) driven by cell ingression in the streak. The same occurs in embryos treated with FGF, where many cells ingress through the circular streak (negative values in the isotropic part of the strain rate), which results in the reorientation of the direction of intercalation of nearby cells perpendicular to the ring (direction of the shear). Presumably, in the LDN case, the cell intercalations continue to occur along the long axis of the mesendoderm (tangential to the ring) because cell ingression and EMT are never activated.

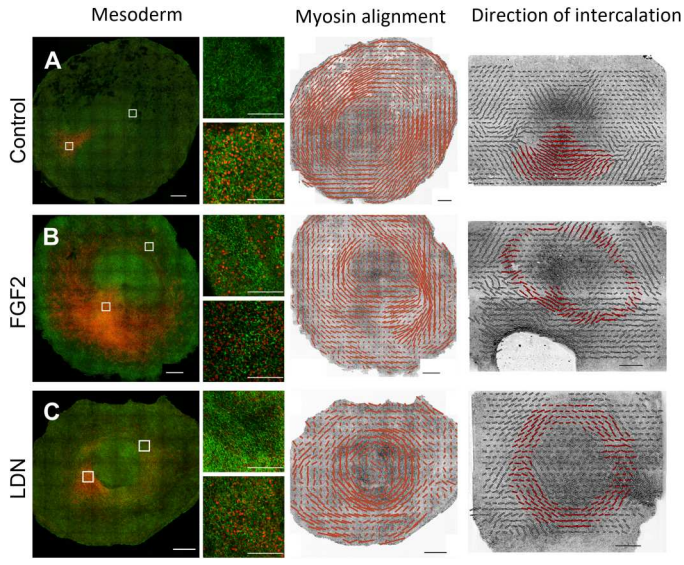

Fig. 4. Comparison of the patterns of mesendoderm differentiation, myosin alignment, and the direction of cell intercalation. Top row: Control embryo after 16 hours of incubation in EC culture as described in Materials and Methods. Second row: Embryo treated with FGF2 for 16 hours. Third row: Embryo treated with LDN (100 nM) for 16 hours (100 nM LDN + 3 μM CHIR for the P tensor). First column: SNAI2$^+$ expression (red) and pMLC (green). The regions in the top and bottom white squares in (**A**) to (**C**) are shown at higher magnification on the right of these images as top and bottom images, respectively. Second main column: The quantitation of myosin cable alignment. Scale bars represent ~30% anisotropy. Third main column: The direction of intercalation calculated as the anisotropic component of the intercalation (P) tensor (*58*). The scale bar represents a magnitude of ~0.4 1/*h*. Regions of intercalating mesendoderm cells are highlighted in red. Scale bars, 500 μm (A to C) and 100 μm (small regions).

A mechanochemical model describes tissue flows: Predictions and implications

To quantify these observations, we propose and explore a theoretical model for gastrulation as a mechanosensitive self-organizing process in the accompanying paper (*19*). Our continuum model couples the myosin-driven tension-sensitive active stress to tissue flow and cable ordering and leads to an interpretation of gastrulation as the result of an instability in the early embryo (fig. S13) (*19*). Our model can recapitulate these different gastrulation modes by varying the extension of the mesendoderm (an initial condition of our model) and a nondimensional parameter modulating the amount of active cell ingression [see figures 2 to 4 and movies 2 to 12 of (*19*)]. Notably, providing only the initial experimental distribution of actomyosin cables′ orientation and active myosin intensity, our model predicts the observed orientation of the cable, the myosin intensity, cell velocities, and velocity divergence at later times without data fitting. The model predicts a strong correlation between the mesendoderm expression domain and myosin planar cell polarity, which persists in the cases of circular mesendoderm domains, as verified with the FGF2 and LDN treatments (fig. S14). By varying the initial mesendoderm domain shape in combination with the degree of myosin-dependent ingression (p0, parameter), this model can also generate the cell flows and DOAs after the various perturbations described here and thus provide a mechanistic understanding of the biophysical mechanisms and role of tissue

stresses and strains involved. For further details on the model and results, see (*19*).

The manipulations described here are sufficient to induce large morphogenetic changes that recapitulate the hallmark dynamics and morphologies of different vertebrate gastrulation modes in a single organism, the chick embryo (Fig. 5). These results suggest that the modulation of the extension of the mesendoderm territory and the presence or absence of EMT controlling cell ingression largely determined the different morphologies observed during the evolution of vertebrate gastrulation.

DISCUSSION

Here, we perturbed the mechanisms that control directed cell intercalations and cell ingressions within the mesendoderm, which generate the forces that drive the tissue flows that generate the primitive streak during chick gastrulation. By targeting FGF, WNT, BMP, and VEGF developmental signaling pathways, known critical regulators of early development, we modulated the size and shape of the mesendoderm territory and uncoupled cell intercalation and ingression.

Our results suggest that FGF may predominantly induce mesoderm precursors, while inhibition of BMP signaling could result in the formation of excess endoderm precursors. These findings could suggest that the differentiation status of the cells affects how these cells internalize. However, it remains unclear whether signaling pathways that control differentiation can modulate cell behaviors, such as cell ingression, independently. Another open question is what is the fate of the cells that are internalized through these ectopic structures and how different internalization modes might affect the cell fate.

The experiments have also shown that directed intercalations along the long axis of the mesendoderm territory are a major part of the mechanism driving the formation of the internalization structure, which is a linear, a circular streak, or a partial or circular blastopore. These cell intercalations are driven by long myosin cables oriented along the long axis of the evolving mesendoderm territory (*15*). We have developed a mechanochemical model that, starting from an initial sickle- or ring-shaped mesendoderm precursor region containing a tension-dependent myosin recruitment mechanism, can explain the emergence of the tissue flows that drive the formation of the primitive streak and predict the dynamics of the domains of ingressing cells, which are in excellent agreement with those experimentally observed, both under normal and experimentally perturbed conditions (*19*). The model has highlighted and elucidated the importance of the mechanochemical feedback of the flow on myosin recruitment and organization of the epiblast tissue flow. However, the mechanisms that set the initial directionality of the myosin cable alignment during normal development and after the experimental perturbations described here resulting in the observed different mesendoderm territories morphologies, sickle or ring, remain to be elucidated.

The purpose of gastrulation is to internalize the mesoderm and endoderm precursors. Unexpectedly, despite being an essential phase of early development, the exact morphology of gastrulation shows considerable variation across the evolutionary tree. Mesoderm and endoderm precursors are typically formed on the surface of the developing embryo from epithelial tissues. Besides

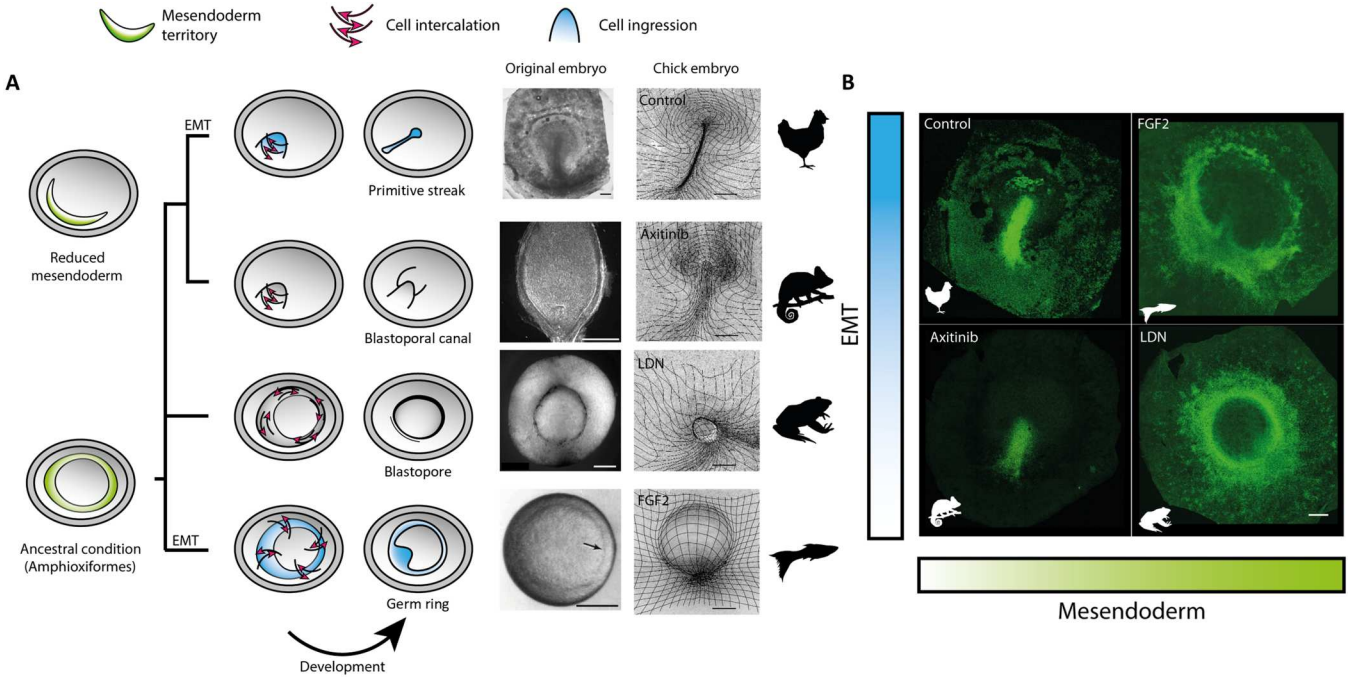

Fig. 5. Changes in the extent of the mesendoderm territory and the degree of EMT could underlie the evolution of vertebrate gastrulation. (**A**) Evolutionary relationships of representative vertebrate morphologies recapitulated in the chick embryo via modification of key cell behaviors. Images of gastrulation showing the blastopoal canal in chameleon (28 days), the blastopore in *Xenopus* (12 hours), and the germ ring in zebrafish (5.7 hours) are adapted from (*33*, *44*, *49*). Scale bars, 250 μm. (**B**) SNAI2^{+} cell distributions in HH3^{+} chick embryos after different treatments show that manipulating the extent of the mesendoderm territory and the level of EMT controlling ingression in the chick embryo reproduce critical morphological structures of gastrulation in other vertebrates. Scale bars, 500 μm (chick embryos).

differences in the shape of the early embryos, spheres (frogs and fish) or sheets (amniotes), and size, there is a great diversity in the mode and geometry of the structures through which the cells internalize (*1*, *2*). In spherical vertebrate embryos, the cells typically internalize through spherical structures such as the germ ring in fish and blastopores in amphibians, while in amniotes, cells internalize a structure known as the primitive streak. Furthermore, cells internalize either through ingression of individual cells, such as in amniotes, or through involution of cells in epithelial sheets, such as in *Xenopus* (*44*), or in a mixed mode as observed in reptiles (*49*).

Our experiments suggest that adjusting the extension of the mesendoderm territory, from a ring to a crescent, and regulating the capacity of these cells to undergo cell ingression are enough to invoke large morphogenetic changes reminiscent of other gastrulation modes. Similarly, it is possible to induce an invaginating gastrulation mode in a fly that normally gastrulates by stochastic individual cell ingression (*Chironomus riparius*) by expressing two genes (folded gastrulation and t48) that are known to control blastoderm invagination during gastrulation in another fly species (*Drosophila melanogaster*) (*59*). In yet another example, it is possible to switch the gastrulation mode of the sea anemone *Nematostella vectensis* from invagination to individual cell ingression by dissociating and reaggregating the cells in the embryo (*60*). Together, these experiments suggest that different gastrulation modes could easily evolve because relatively small quantitative changes in signaling, gene expression, or the developmental context can drive major morphogenetic transitions through their effects on the modulation of individual cell behaviors.

MATERIALS AND METHODS

Chemicals and other reagents

LDN, CHIR, axitinib, and SB50124 were acquired from Sigma-Aldrich. Hydromount was obtained from National Diagnostics. Ultrapure grade was acquired from Merck/VWR. Recombinant human FGF2 (233-FB) and recombinant human VEGFR2/KDR-Fc (357-KD-050) were obtained from (R&D Systems). Primary antibodies phospho-myosin light chain 2 (S19) mouse monoclonal antibody (mAb) (3675), phospho-myosin light chain 2 (T18, S19) rabbit mAb (3674), and SNAI2 (C19G7) rabbit mAb (9585) were from Cell Signaling Technology. The TNC mouse mAb M1-B4 and the Hnf3β/FoxA2 mAb 4C7 were from the Developmental Studies Hybridoma Bank. Alexa fluorophore-conjugated secondary antibodies were obtained from Invitrogen.

Chick lines and embryo culture

Fertile eggs from white Leghorn chicks were obtained from Henry Stewart & Co., Lincolnshire, UK. Membrane GFP embryos were obtained from the National Avian Research facility at Edinburgh University. Embryos were cultured using the Embryo Culture method according to published procedures (*61*).

Imaging

To image the complete chick embryo during gastrulation, we use a chick line expressing GFP in the cell membranes (myr-GFP) and a dedicated light sheet microscope as described in detail in (*15*). To cover the entire embryo (~4 mm in diameter), we acquire images at intervals of 1.84 μm at 45° with respect to the surface in two overlapping sequential scans (~5000 images of 2560 × 400 pixels), covering roughly an area of 3.2 mm by 4.7 mm every 3 min. Embryos are cultured during imaging as described in (*42*). Under these conditions, chick embryos can develop for more than 24 hours at 37°C (480 time points, >2 terabytes).

Image processing

Surface focusing

First, we transform the image volumes from the original 45° geometry to a 90° geometry. Once the image volumes have been transformed, we find the surface using a method based on the square gradient focusing algorithm (*62*, *63*). Briefly, we tile the volume in 25 × 25 pixel columns and use the algorithm to find the position of the surface in each column, which constitutes the height map. Last, we apply a smoothing filter to the height map and use this to section the image volume to produce a two-dimensional image of the surface of the embryo (fig. S1A).

Velocity fields and strain rates

The velocity fields at the surface of the embryo are computed by digital PIV (fig. S1B) using PIVLab vs1.32 for MATLAB with two passes of 64 × 64 pixels and 32 × 32 pixels with a 50% overlap as in (*15*). The gradient of the velocity can be used to compute the strain rate at the surface of the embryo. They can be decomposed into two parts: the isotropic term, which describes the local rate of change in the area, and the anisotropic term, which describes the local rate of shear deformation. Together, they can be used as an indirect but robust measure of cell behaviors. In a confluent epithelial sheet, as the epiblast, the isotropic term is the product of the balance of changes in the cell area, cell divisions, and cell ingressions. In contrast, the anisotropic part is the result of directed cell intercalation or coordinated asymmetric changes in cell shape (fig. S1C). The implementation details can be found in (*15*).

Division detection

We developed a robust algorithm to detect and track individual cell divisions independently of image segmentation (*63*). During cytokinesis, epithelial cells round up on the surface, acquiring a very typical circular shape. We used the circular Hough transform implementation in MATLAB to find the characteristic circular shapes associated with dividing cells. The algorithm uses PIV to follow the dividing cells to avoid counting the same division event repeatedly between consecutive frames.

Myosin quantification

To quantify the myosin concentration and alignment, the position of the apical epiblast surface needs to be identified. To achieve this more reliably, we used the stronger actin signal to find the precise location of the apical surface using the above-described method (fig. S1, E and F). This surface projection was analyzed for myosin anisotropy using a Fourier transform–based algorithm (fig. S1G) (*64*) to find cellular anisotropy and size using a subtiling of the surface in 256 × 256 pixels and a 50% overlap between tiles.

Chemical manipulations

For in vivo imaging, the embryos were later transferred to imaging chambers as described in (*65*), and the chemical inhibitors were dissolved in the 10-ml albumen that covers the embryos during imaging. For immunocytochemistry experiments, chemical inhibitors were dissolved in the EC culture substrate. Recombinant human FGF2 and VEGFR2-Fc were added as a 1-μl drop (50 μg/ml) and carefully deposited on the hypoblast side of embryos in EC culture. For life imaging, the embryos were later transferred to

imaging chambers maintaining the added protein on the hypoblast side of the embryo. All experiments were repeated two to three times, and each experiment typically contained six to eight embryos per treatment and six to eight internal control embryos to score variations in development success and timing between different batches of fertilized eggs obtained at different periods during the year.

Immunocytochemistry

After the chemical manipulations, the embryos were fixed in 4% paraformaldehyde/phosphate-buffered saline (PBS) containing 0.1% Tween 20 on ice for 3 hours and later washed three times in PBS. Later, antibody detection was performed as described (*15*) followed by staining with 4′,6-diamidino-2-phenylindole and Alexa 405 Phalloidin. Embryos were mounted in Hydromount and imaged using a wide-field microscope or a Leica TCS SP8 confocal microscope at ×10 to ×20 magnifications. Selected embryos were processed for sectioning; first, embryos were embedded in 7.5% gelatin/15% sucrose, followed by freezing in a dry ice/isopentane mixture, and sectioned on a Leica cryostat. Sections were mounted on lysine-coated microscope slides and mounted with Hydromount.

Confocal microscopy

To image the embryos, confocal tile scans were taken at ×10 and ×20 magnifications using sequential line scanning on a Leica SP8 confocal microscope. To cover the thickness of the embryo, stacks of 20 to 40 slices were taken at 2- to 4-μm intervals along the z axis.

Dynamic morphoskeletons

Given a planar velocity field $\mathbf{v}(\mathbf{x}, t)$, we compute the DM from the backward and forward finite-time Lyapunov exponents (FTLEs) (*18*). We compute the FTLE as

$$\Lambda_{t_0}^{t_f}(\mathbf{x_0}) = \frac{\ln[\lambda_2(\boldsymbol{x_0})]}{\mid t_f - t_0 \mid}, \quad \boldsymbol{x_f} := \boldsymbol{F}_{t_0}^{t_f}(\boldsymbol{x_0}) = \boldsymbol{x_0} + \int_{t_0}^{t_f} \boldsymbol{v}[\boldsymbol{F}_{t_0}^{\tau}(\boldsymbol{x_0}), \tau] \quad (1)$$

where $\lambda_2(x_0)$ denotes the highest singular value of the Jacobian of the flow map $F_{t_0}^{t_f}(x_0)$ and the flow map describing the trajectories from their initial x_0 to final x_f positions. To compute the FTLE, we first calculate $F_{t_0}^{t}(x_0)$ by integrating the cell velocity field $v(x, t)$ using the MATLAB built-in Runge-Kutta solver ODE45 with an absolute and relative tolerance of 10^{-6}, linear interpolation in space and time, and a uniform dense grid of the initial conditions. Then, denoting the ith component of the flow map $\boldsymbol{F}_{t_0}^{t}(\boldsymbol{x_0})$ by $x^i(x_0^1, x_0^2, t_0, t)$, we compute the deformation gradient $\nabla \boldsymbol{F}_{t_0}^{t}(\boldsymbol{x_0})$ using the finite-difference approximation

$$\nabla \boldsymbol{F}_{t_0}^{t}(\boldsymbol{x_0}) \approx \begin{bmatrix} \frac{x^1(x_0^1+\delta, x_0^2, t_0, t) - x^1(x_0^1-\delta, x_0^2, t_0, t)}{2\delta} & \frac{x^1(x_0^1, x_0^2+\delta, t_0, t) - x^1(x_0^1, x_0^2-\delta, t_0, t)}{2\delta} \\ \frac{x^2(x_0^1+\delta, x_0^2, t_0, t) - x^2(x_0^1-\delta, x_0^2, t_0, t)}{2\delta} & \frac{x^2(x_0^1, x_0^2+\delta, t_0, t) - x^2(x_0^1, x_0^2-\delta, t_0, t)}{2\delta} \end{bmatrix} \quad (2)$$

where δ is the initial conditions′ grid spacing. After computing $\boldsymbol{F}_{t_0}^{t}(\boldsymbol{x_0})$, we use Eq. 1 for computing the FTLE field.

Supplementary Materials

This PDF file includes:
Figs. S1 to S14

Other Supplementary Material for this manuscript includes the following:
Movies S1 to S11

View/request a protocol for this paper from *Bio-protocol*.

REFERENCES AND NOTES

1. C. D. Stern, *Gastrulation: From Cells to Embryo* (CSHL Press, 2004).
2. D. Arendt, K. Nübler-Jung, Rearranging gastrulation in the name of yolk: Evolution of gastrulation in yolk-rich amniote eggs. *Mech. Dev.* **81**, 3–22 (1999).
3. L. Solnica-Krezel, *Gastrulation: From Embryonic Pattern to Form* (Academic Press, 2020).
4. R. Keller, Shaping the vertebrate body plan by polarized embryonic cell movements. *Science* **298**, 1950–1954 (2002).
5. M. Williams, C. Burdsal, A. Periasamy, M. Lewandoski, A. Sutherland, Mouse primitive streak forms in situ by initiation of epithelial to mesenchymal transition without migration of a cell population. *Dev. Dyn.* **241**, 270–283 (2012).
6. D. Kimelman, Mesoderm induction: From caps to chips. *Nat. Rev. Genet.* **7**, 360–372 (2006).
7. T. Merle, E. Farge, Trans-scale mechanotransductive cascade of biochemical and biomechanical patterning in embryonic development: The light side of the force. *Curr. Opin. Cell Biol.* **55**, 111–118 (2018).
8. P.-F. Lenne, E. Munro, I. Heemskerk, A. Warmflash, L. Bocanegra-Moreno, K. Kishi, A. Kicheva, Y. Long, A. Fruleux, A. Boudaoud, Roadmap for the multiscale coupling of biochemical and mechanical signals during development. *Phys. Biol.* **18**, 041501 (2021).
9. G. Sheng, A. M. Arias, A. Sutherland, The primitive streak and cellular principles of building an amniote body through gastrulation. *Science* **374**, eabg1727 (2021).
10. M. Valet, E. D. Siggia, A. H. Brivanlou, Mechanical regulation of early vertebrate embryogenesis. *Nat. Rev. Mol. Cell Biol.* **23**, 169–184 (2022).
11. T. Brunet, A. Bouclet, P. Ahmadi, D. Mitrossilis, B. Driquez, A.-C. Brunet, L. Henry, F. Serman, G. Béalle, C. Ménager, F. Dumas-Bouchiat, D. Givord, C. Yanicostas, D. Le-Roy, N. M. Dempsey, A. Plessis, E. Farge, Evolutionary conservation of early mesoderm specification by mechanotransduction in Bilateria. *Nat. Commun.* , 1–15 (2013).
12. E. Hannezo, C.-P. Heisenberg, Mechanochemical feedback loops in development and disease. *Cell* **178**, 12–25 (2019).
13. Y. Maroudas-Sacks, K. Keren, Mechanical patterning in animal morphogenesis. *Annu. Rev. Cell Dev. Biol.* **37**, 469–493 (2021).
14. C. Collinet, T. Lecuit, Programmed and self-organized flow of information during morphogenesis. *Nat. Rev. Mol. Cell Biol.* **22**, 245–265 (2021).
15. E. Rozbicki, M. Chuai, A. I. Karjalainen, F. Song, H. M. Sang, R. Martin, H. J. Knolker, M. P. MacDonald, C. J. Weijer, Myosin-II-mediated cell shape changes and cell intercalation contribute to primitive streak formation. *Nat. Cell Biol.* **17**, 397–408 (2015).
16. O. Voiculescu, L. Bodenstein, I. J. Lau, C. D. Stern, Local cell interactions and self-amplifying individual cell ingression drive amniote gastrulation. *eLife* **3**, e01817 (2014).
17. G. Serrano Nájera, C. J. Weijer, Cellular processes driving gastrulation in the avian embryo. *Mech. Dev.* **163**, 103624 (2020).
18. M. Serra, S. Streichan, M. Chuai, C. J. Weijer, Dynamic morphoskeletons in development. *Proc. Natl. Acad. Sci. U.S.A.* **117**, 11444–11449 (2020).
19. M. Serra, G. Serrano Nájera, M. Chuai, V. Spandan, C. J. Weijer, L. Mahadevan, A mechanochemical model recapitulates distinct vertebrate gastrulation modes. bioRxiv 2021.10.03.462928 (2021).https://doi.org/10.1101/2021.10.03.462928.
20. C. Alev, Y. Wu, Y. Nakaya, G. Sheng, Decoupling of amniote gastrulation and streak formation reveals a morphogenetic unity in vertebrate mesoderm induction. *Development* **140**, 2691–2696 (2013).
21. O. Voiculescu, F. Bertocchini, L. Wolpert, R. E. Keller, C. D. Stern, The amniote primitive streak is defined by epithelial cell intercalation before gastrulation. *Nature* **449**, 1049–1052 (2007).
22. M. Saadaoui, D. Rocancourt, J. Roussel, F. Corson, J. Gros, A tensile ring drives tissue flows to shape the gastrulating amniote embryo. *Science* **367**, 453–458 (2020).
23. L. Gräper, Die Primitiventwicklung des Hühnchens nach stereokinematographischen Untersuchungen, kontrolliert durch vitale Farbmarkierung und verglichen mit der Entwicklung anderer Wirbeltiere. *Dev. Genes Evol.* **116**, 382–429 (1929).
24. M. Chuai, W. Zeng, X. Yang, V. Boychenko, J. A. Glazier, C. J. Weijer, Cell movement during chick primitive streak formation. *Dev. Biol.* **296**, 137–149 (2006).
25. Y. Nakaya, E. W. Sukowati, Y. Wu, G. Sheng, RhoA and microtubule dynamics control cell-basement membrane interaction in EMT during gastrulation. *Nat. Cell Biol.* **10**, 765–775 (2008).
26. Y. Hatada, C. D. Stern, A fate map of the epiblast of the early chick embryo. *Development* **120**, 2879–2889 (1994).

27. X. Yang, H. Chrisman, C. J. Weijer, PDGF signalling controls the migration of mesoderm cells during chick gastrulation by regulating N-cadherin expression. *Development* **135**, 3521–3530 (2008).
28. M. A. Selleck, C. D. Stern, Fate mapping and cell lineage analysis of Hensen's node in the chick embryo. *Development* **112**, 615–626 (1991).
29. X. Yang, D. Dormann, A. E. Munsterberg, C. J. Weijer, Cell movement patterns during gastrulation in the chick are controlled by positive and negative chemotaxis mediated by FGF4 and FGF8. *Dev. Cell* **3**, 425–437 (2002).
30. A. Lawson, G. C. Schoenwolf, Epiblast and primitive-streak origins of the endoderm in the gastrulating chick embryo. *Development* **130**, 3491–3501 (2003).
31. G. Zhao, W. Li, D. Chen, J. R. Henry, H.-Y. Li, Z. Chen, M. Zia-Ebrahimi, L. Bloem, Y. Zhai, K. Huss, A novel, selective inhibitor of fibroblast growth factor receptors that shows a potent broad spectrum of antitumor activity in several tumor xenograft models. *Mol. Cancer Ther.* **10**, 2200–2210 (2011).
32. H. Acloque, O. H. Ocana, A. Matheu, K. Rizzoti, C. Wise, R. Lovell-Badge, M. A. Nieto, Reciprocal repression between Sox3 and snail transcription factors defines embryonic territories at gastrulation. *Dev. Cell* **21**, 546–558 (2011).
33. C. B. Kimmel, W. W. Ballard, S. R. Kimmel, B. Ullmann, T. F. Schilling, Stages of embryonic development of the zebrafish. *Dev. Dyn.* **203**, 253–310 (1995).
34. J. P. Trinkaus, Ingression during early gastrulation of Fundulus. *Dev. Biol.* **177**, 356–370 (1996).
35. L. A. Rohde, C.-P. Heisenberg, Zebrafish gastrulation: Cell movements, signals, and mechanisms. *Int. Rev. Cytol.* **261**, 159–192 (2007).
36. D. Pinheiro, C.-P. Heisenberg, Zebrafish gastrulation: Putting fate in motion. *Curr. Top. Dev. Biol.* **136**, 343–375 (2020).
37. A. Streit, K. J. Lee, I. Woo, C. Roberts, T. M. Jessell, C. D. Stern, Chordin regulates primitive streak development and the stability of induced neural cells, but is not sufficient for neural induction in the chick embryo. *Development* **125**, 507–519 (1998).
38. F. Bertocchini, C. D. Stern, Gata2 provides an early anterior bias and uncovers a global positioning system for polarity in the amniote embryo. *Development* **139**, 4232–4238 (2012).
39. H. C. Lee, H.-C. Lu, M. Turmaine, N. M. M. Oliveira, Y. Yang, I. De Almeida, C. D. Stern, Molecular anatomy of the pre-primitive-streak chick embryo. *Open Biol.* **10**, 190299 (2020).
40. C. F. Arias, M. A. Herrero, C. D. Stern, F. Bertocchini, A molecular mechanism of symmetry breaking in the early chick embryo. *Sci. Rep.* **7**, 15776 (2017).
41. G. Sanchez-Duffhues, E. Williams, M. J. Goumans, C. H. Heldin, P. ten Dijke, Bone morphogenetic protein receptors: Structure, function and targeting by selective small molecule kinase inhibitors. *Bone* **138**, 115472 (2020).
42. E. Rozbicki, M. Chuai, C. J. Weijer, Technique for liquid culture of early chick embryos suitable for long term live imaging (Research Square, 2015).
43. J. Chal, Z. Al Tanoury, M. Hestin, B. Gobert, S. Aivio, A. Hick, T. Cherrier, A. P. Nesmith, K. K. Parker, O. Pourquié, Generation of human muscle fibers and satellite-like cells from human pluripotent stem cells in vitro. *Nat. Protoc.* **11**, 1833–1850 (2016).
44. D. R. Shook, E. M. Kasprowicz, L. A. Davidson, R. Keller, Large, long range tensile forces drive convergence during *Xenopus* blastopore closure and body axis elongation. *eLife* 7, e26944 (2018).
45. A. Eichmann, C. Corbel, V. Nataf, P. Vaigot, C. Bréant, N. M. Le Douarin, Ligand-dependent development of the endothelial and hemopoietic lineages from embryonic mesodermal cells expressing vascular endothelial growth factor receptor 2. *Proc. Natl. Acad. Sci. U.S.A.* **94**, 5141–5146 (1997).
46. M. Chuai, D. Hughes, C. J. Weijer, Collective epithelial and mesenchymal cell migration during gastrulation. *Curr. Genomics* **13**, 267–277 (2012).
47. J. Ma, D. J. Waxman, Modulation of the antitumor activity of metronomic cyclophosphamide by the angiogenesis inhibitor axitinib. *Mol. Cancer Ther.* **7**, 79–89 (2008).
48. J. Firmino, D. Rocancourt, M. Saadaoui, C. Moreau, J. Gros, Cell division drives epithelial cell rearrangements during gastrulation in chick. *Dev. Cell* **36**, 249–261 (2016).
49. M. J. Stower, R. E. Diaz, L. C. Fernandez, M. W. Crother, B. Crother, A. Marco, P. A. Trainor, S. Srinivas, F. Bertocchini, Bi-modal strategy of gastrulation in reptiles. *Dev. Dyn.* **244**, 1144–1157 (2015).
50. M. J. Stower, F. Bertocchini, The evolution of amniote gastrulation: The blastopore-primitive streak transition. *Wiley Interdiscip. Rev. Dev. Biol.* **6**, 1–17 (2017).
51. K. Mogi, R. Toyoizumi, Invasion by matrix metalloproteinase-expressing cells is important for primitive streak formation in early chick blastoderm. *Cells Tissues Organs* **192**, 1–16 (2010).
52. K. L. Crossin, S. Hoffman, M. Grumet, J. P. Thiery, G. M. Edelman, Site-restricted expression of cytotactin during development of the chicken embryo. *J. Cell Biol.* **102**, 1917–1930 (1986).
53. Y. Nakaya, G. Sheng, An amicable separation: Chick's way of doing EMT. *Cell Adh. Migr.* **3**, 160–163 (2009).
54. C. Kyprianou, N. Christodoulou, R. S. Hamilton, W. Nahaboo, D. S. Boomgaard, G. Amadei, I. Migeotte, M. Zernicka-Goetz, Basement membrane remodelling regulates mouse embryogenesis. *Nature* **582**, 253–258 (2020).
55. S. C. Chapman, F. R. Schubert, G. C. Schoenwolf, A. Lumsden, Analysis of spatial and temporal gene expression patterns in blastula and gastrula stage chick embryos. *Dev. Biol.* **245**, 187–199 (2002).
56. S. C. Chapman, K. Matsumoto, Q. Cai, G. C. Schoenwolf, Specification of germ layer identity in the chick gastrula. *BMC Dev. Biol.* **7**, 1–16 (2007).
57. I. Burtscher, H. Lickert, Foxa2 regulates polarity and epithelialization in the endoderm germ layer of the mouse embryo. *Development* **136**, 1029–1038 (2009).
58. F. Graner, B. Dollet, C. Raufaste, P. Marmottant, Discrete rearranging disordered patterns, part I: Robust statistical tools in two or three dimensions. *Eur. Phys. J. E* **25**, 349–369 (2008).
59. S. Urbansky, P. G. Avalos, M. Wosch, S. Lemke, Folded gastrulation and T48 drive the evolution of coordinated mesoderm internalization in flies. *eLife* **5**, e18318 (2016).
60. K. Anastasia, G. Grigory, P. Ekaterina, D. Adrien, K. Yulia, T. Ulrich, Germ-layer commitment and axis formation in sea anemone embryonic cell aggregates. *Proc. Natl. Acad. Sci. U.S.A.* **115**, 1813–1818 (2018).
61. S. C. Chapman, J. Collignon, G. C. Schoenwolf, A. Lumsden, Improved method for chick whole-embryo culture using a filter paper carrier. *Dev. Dyn.* **220**, 284–289 (2001).
62. A. M. Eskicioglu, P. S. Fisher, Image quality measures and their performance. *IEEE Trans. Commun.* **43**, 2959–2965 (1995).
63. G. Serrano Nájera, thesis, University of Dundee (2021).
64. M. Durande, S. Tlili, T. Homan, B. Guirao, F. Graner, H. Delanoe-Ayari, Fast determination of coarse-grained cell anisotropy and size in epithelial tissue images using Fourier transform. *Phys. Rev. E* **99**, 62401 (2019).
65. E. Rozbicki, M. Chuai, C. J. Weijer, Liquid culture technique for early chick embryos suitable for long term live imaging. *Nat. Protoc. Exchange*2015). 10.1038/protex.2015.012.

Acknowledgments

Funding: This work was supported by the EASTBIO BBSRC PhD student training grant 1785593 (to G.S.N.); Swiss National Foundation, Schmidt Science Fellowship, and the Postdoc Mobility Fellowship (to M.S.); NSF-Simons Center for Mathematical and Statistical Analysis of Biology Award 1764269 (to L.M.); NIH 1R01HD097068 (to L.M.); Simons Foundation (to L.M.); Henri Seydoux Fund (to L.M.); BBSRC grants BB/N009789/1, BB/K00204X/1, BB/R000441/1, BB/T006781/1 (to C.J.W.); and Wellcome Trust: Imaging equipment award 101468/Z/13/Z (to C.J.W.). **Author contributions:** Conceptualization: M.C., G.S.N., M.S., L.M., and C.J.W. Methodology: M.C., G.S.N., M.S., and C.J.W. Investigation: M.C., G.S.N., and M.S. Supervision: L.M. and C.J.W. Writing—original draft: G.S.N. and C.J.W. Writing—review and editing: M.C., G.S.N., M.S., L.M., and C.J.W. **Competing interests:** The authors declare that they have no competing interests. **Data and materials availability:** High-resolution images of confocal data and the original high-resolution images from the light sheet microscopy (movies S1, S4, S7, and S9) have been deposited in the BioImage Archive under accession number S-BIAD553 (www.ebi.ac.uk/biostudies/BioImages/studies/S-BIAD553). Higher-resolution versions of movies S1 to S11 are available at https://doi.org/10.15132/10000190. All other data needed to evaluate the conclusions in the paper are present in the paper and/or the Supplementary Materials.

Submitted 3 December 2021
Accepted 28 November 2022
Published 4 January 2023
10.1126/sciadv.abn5429

ScienceAdvances

Reconstruction of distinct vertebrate gastrulation modes via modulation of key cell behaviors in the chick embryo

Manli ChuaiGuillermo Serrano NájeraMattia SerraLakshminarayanan MahadevanCornelis J. Weijer

Sci. Adv., 9 (1), eabn5429. • DOI: 10.1126/sciadv.abn5429

Science Advances (ISSN) is published by the American Association for the Advancement of Science. 1200 New York Avenue NW, Washington, DC 20005. The title *Science Advances* is a registered trademark of AAAS.

Science Advances
AAAS

Supplementary Materials for

Reconstruction of distinct vertebrate gastrulation modes via modulation of key cell behaviors in the chick embryo

Manli Chuai *et al.*

Corresponding author: Guillermo Serrano Nájera, gs714@cam.ac.uk; Cornelis J. Weijer, c.j.weijer@dundee.ac.uk

Sci. Adv. **9**, eabn5429 (2023)
DOI: 10.1126/sciadv.abn5429

The PDF file includes:

Other Supplementary Material for this manuscript includes the following:

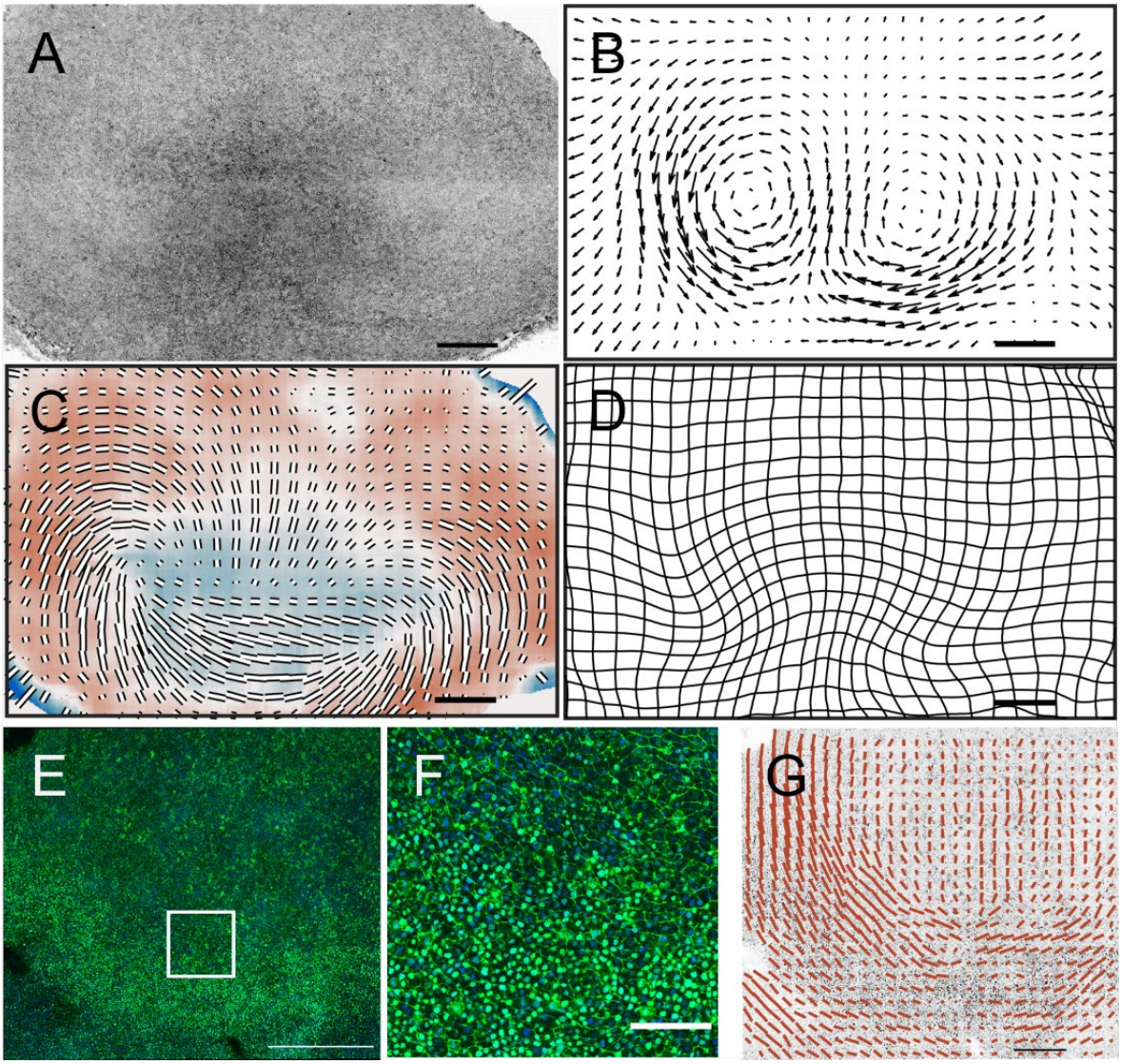

Fig. S1. Correlation of tissue flow, deformation speed, cell shape, and myosin distribution and alignment. **(A**) Epiblast view of HH2 stage embryo in light sheet microscope (**B**) Velocity field for the embryo (HH2) shown in A. (**C**) Strain rate tensor, isotropic component color coded red-blue, the anisotropic component is shown as black bars in direction of contraction. (**D**) Deformation grid calculated from stage HH1 to current stage HH2 for embryo shown in A. D: SNAI and phosphor-myosin light chain in HH2 stage embryo. (**E**) Overview image of pMLC and SNAI2 straining in the posterior region of an HH2 embryo. (**F**) High magnification image of section in the white box shown in E showing myosin cables and nuclear SNAI staining. **(G)** Myosin anisotropy computed for embryo shown in E. Scale bars in A-F 500 μm. In C the scale bar length represents ~ 0.5 1/h for the anisotropic component of the strain rate. In G the scale bar represents 250 μm and ~ 70% anisotropy.

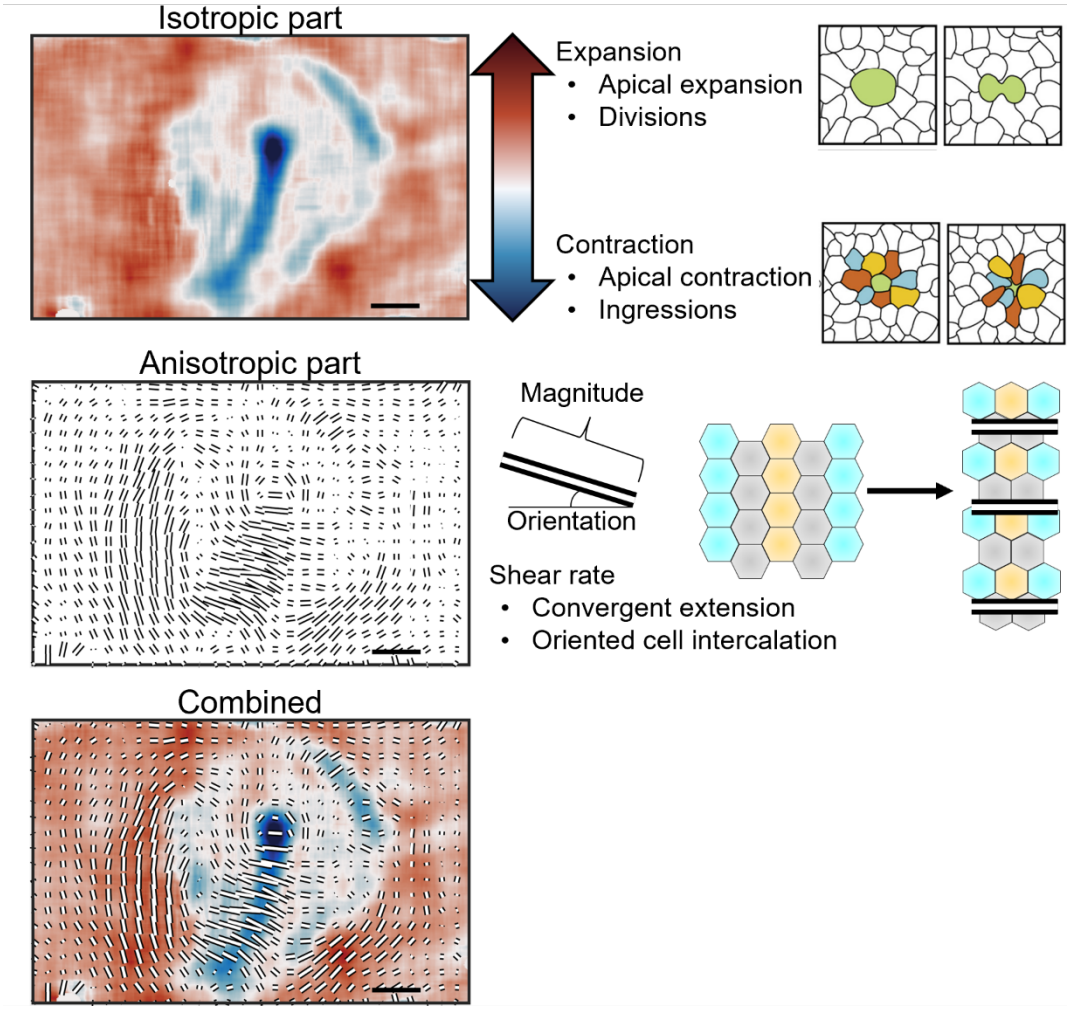

Fig. S2. The decomposed strain rate tensor indicates the cell behaviors underlying the tissue flows on a continuous epithelial layer. Top, The Isotropic part of the strain rate describes how the tissue is changing in the area. Positive values (red) indicate tissue expansion, produced by a combination of apical expansion and cell proliferation. Negative values (blue) indicate contraction, produced by apical contraction and cell ingressions. Middle: The anisotropic part of the strain rate tensor represents the rate of pure shear deformation. The orientation of the bars indicates that the tissue is contracting along the bar while expanding in the perpendicular direction without changing the area. The length of the bar represents the magnitude of the shear deformation rate. In the chick embryo, most of the shear rate is explained by oriented cell intercalations (15). Bottom: The combination of the isotropic and anisotropic components of the strain rate provides a clear indication of the key cell behaviors underlying the tissue flows.

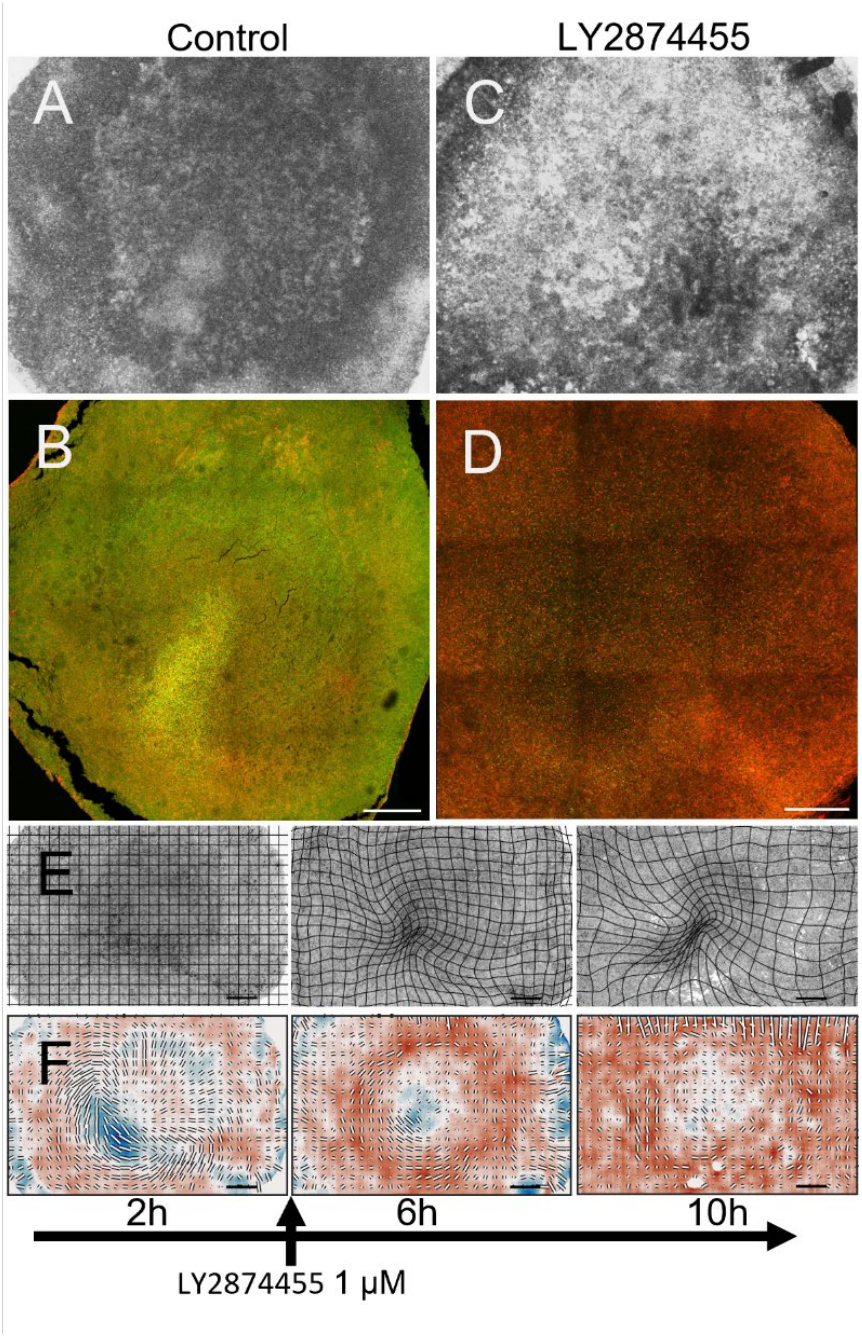

Fig. S3. Inhibition of FGF signaling blocks mesoderm differentiation and streak formation. (**A)**, surface view of control embryo after 16hrs of development in EC culture. (**B**), Composite confocal imager of SNAI (green) and actin (red) of the embryo is shown in A. (**C**), Embryo after 16hrs of treatment with the FGF receptor inhibitor LY2874455 (1uM). (**D**), Composite confocal imager of SNAI (green) and actin (red) of the embryo shown in C, showing absence of SNAI expression. (**E)**, Three successive times of embryo images in light sheet 4, 8, and 12 hours faster addition of LY2874455 (1uM). Note that LY2874455 treated embryos fail in generating a primitive streak (3/3 in the light sheet microscope). (**F**), strain rate tensor at 4,8 and 12 hours for embryo shown in C. Scale bars for E and F as in Fig. S1 C.

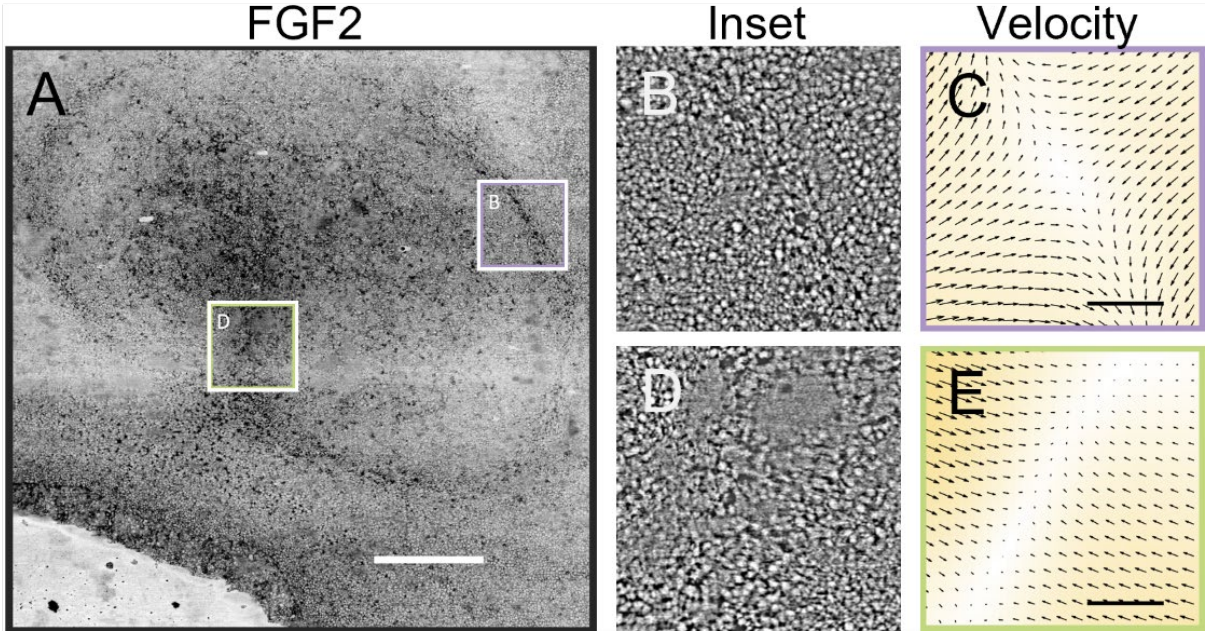

Fig. S4. **Convergent extension on the circular primitive streak generated by FGF2 addition.** (**A**), Overview images of embryo treated with FGF (50 µg/mL) from light sheet microscope after 13h. (**B**), Close up of the circular primitive streak generated by FGF addition (see Movie S4). (**C**), Velocity field calculated on B shows convergence extension flows along the circular primitive streak. (**D**), Close-up of the original primitive streak. (**E**), Velocity field calculated on D showing convergence extension flows along the original primitive streak.

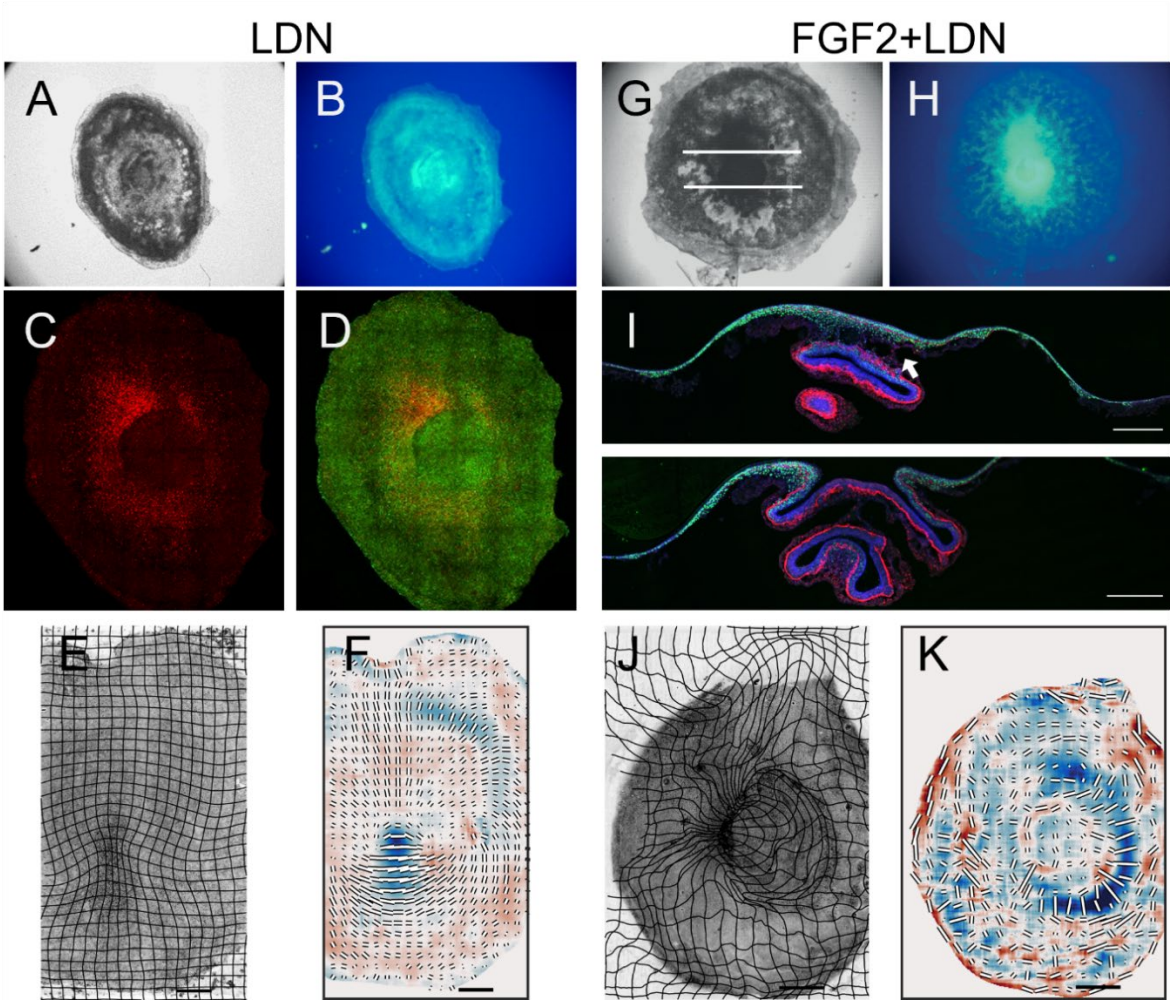

Fig. S5 Changes in gastrulation morphology after interfering with BMP and FGF signaling. (A), widefield image of embryo treated for 16hrs with LDN-193189 for 16hrs. (**B**), Widefield image of (S19)phospho-myosin light chain expression of the embryo shown in A. (**C**), Confocal image of SNAI expression of the embryo shown in A. (**D**), Confocal image of (S19) phospho-myosin light chain and SNAI expression in embryo shown in A. (**E**), light sheet microscopy images of an embryo treated with LDN-193189 (100nM) for 10 hours. (**F**), Strain rate tensor for embryo shown in E. Typically, LDN-193189 treated embryos (100nM) generate a large depression at the boundary between the epiblast, and the consequent invagination of the central epiblast, that results in the detachment of the embryo from the vitelline membrane when cultured in the light-sheet microscope (5/5 embryos in the light sheet microscope). (**G**), Widefield image of an embryo after treatment of LDN-193189 and FGF2 for 16hrs. (**H**), Widefield image of (S19)phospho-myosin light chain expression of the embryo shown in G. (**I**), Two sections through embryo shown in G at the position of white lines. (**J**), Lightsheet microscopy images of embryo treated with LDN-193189 (100nM) and FGF2 (50 µg/mL) for 15 hours. (**K**), Strain rate tensor for embryo shown in J. In LDN-193189 + FGF2 the LDN-193189 phenotype dominates at the morphogenetic level, generating a large invagination that engulfs the epiblast (6/7 embryos in the lightsheet microscope). Scale bars as in figure 1, except in I where the scale bars are 250 μm. Scale bar for K as in Fig. S1 C.

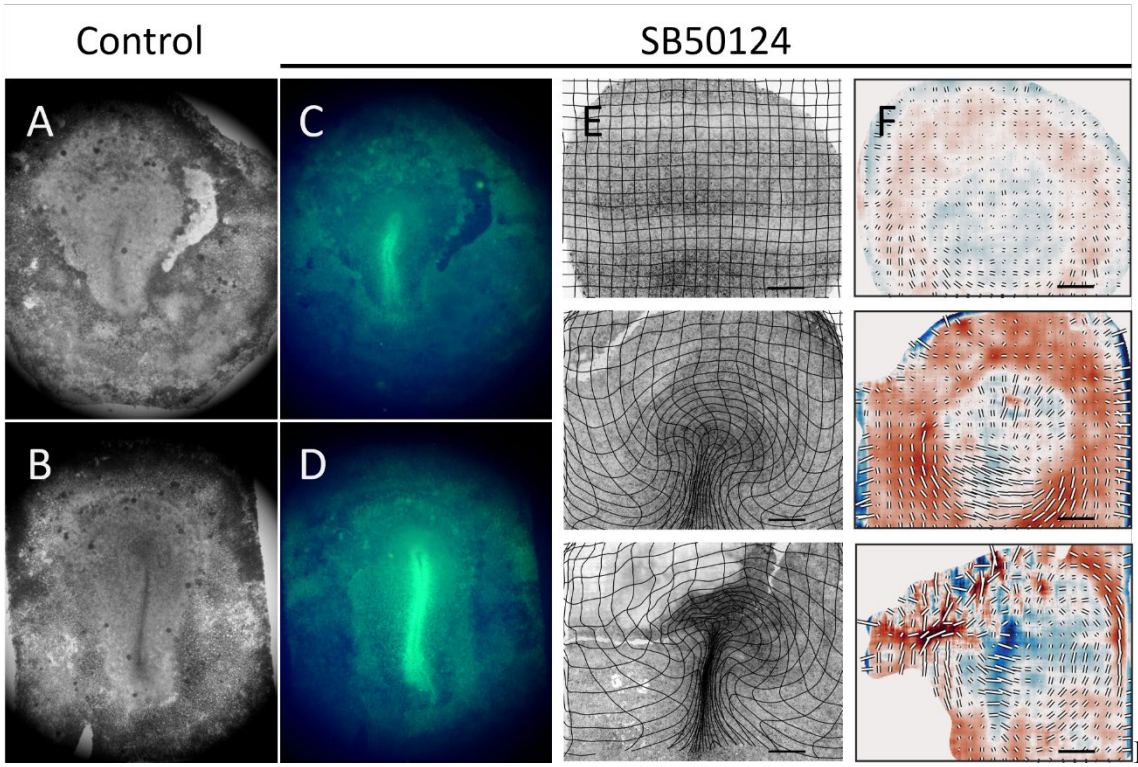

Fig. S6 Inhibition of Nodal signaling partly inhibits streak formation. (**A**), widefield image of control embryo after 16hrs development in EC culture**. (B**), Embryo after 16hrs incubation in EC culture with the Nodal signaling inhibitor SB50124 (10 μM). (**C**), SNAI expression in embryo shown in A. (**D**), SNAI expression in embryo shown in A. (**E**), Surface view of embryo in light sheet microscope 2, 4, and 8 hours (from top to bottom) the after addition of SB50124 (10 μM). (**F**), Strain rate tensor of the embryo at successive times shown in E (2/2 in the light sheet microscope). Scale bars 500 μm. Scale bars for F as in Fig. S1 C.

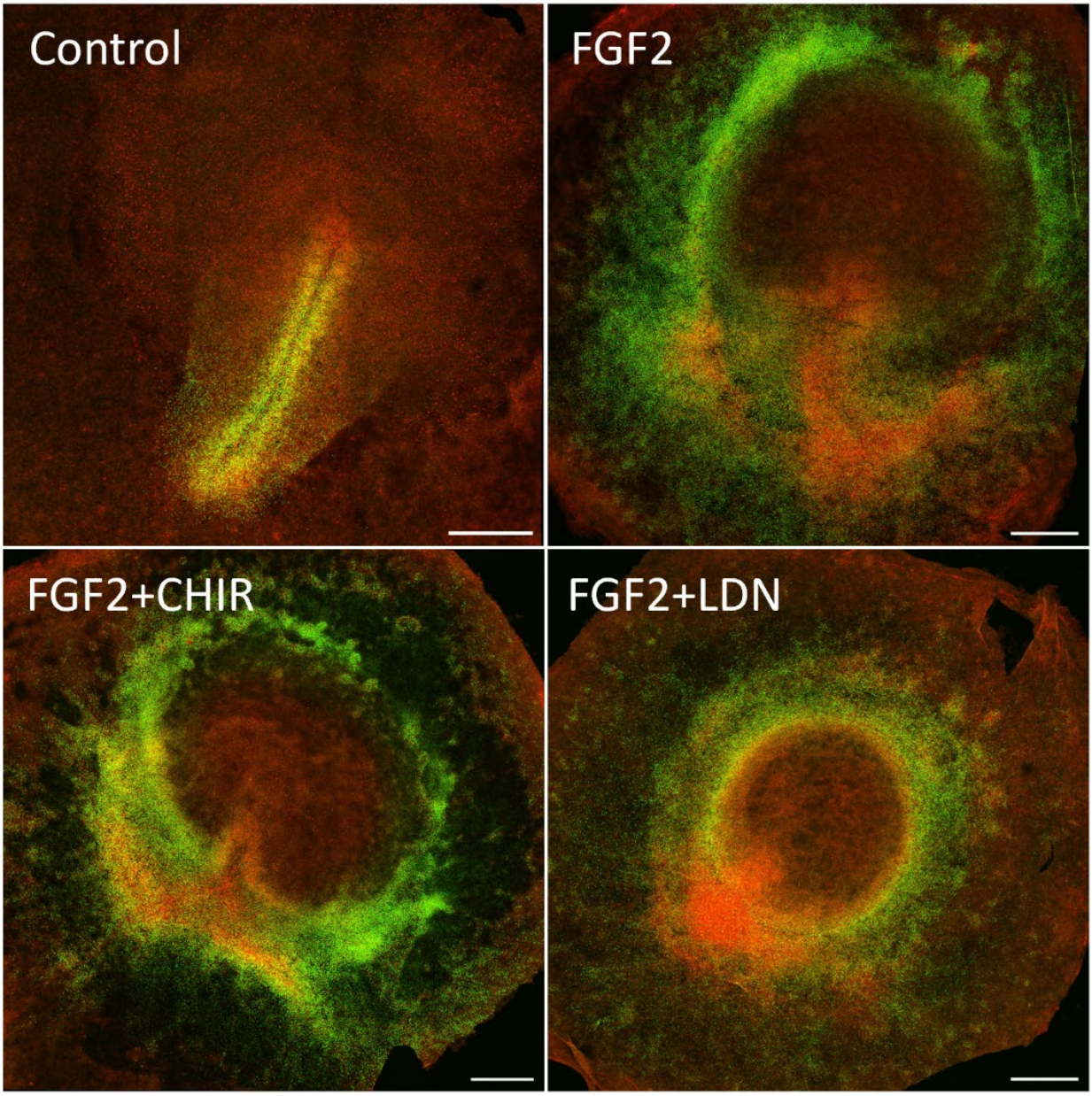

Fig. S7 Effect of perturbation of different signaling pathways on mesoderm formation and Localisation. Merged images showing SNAI2 expression (green) and actin (red) localization after 16hrs of varying treatments as indicated in legends. Control experiments show that the very tip of the streak is devoid of SNAI2 expression. FGF treatment results in a ring of mesoderm expression at the embryonic extraembryonic interface. Combined FGF and CHIR treatment results in very similar phenotypes as FGF alone. FGF treatment combined with inhibition of BMP signaling reinforces mesoderm differentiation in the ring and results in tissue buckling and suppresses streak formation and extension. Scale bars 500µm.

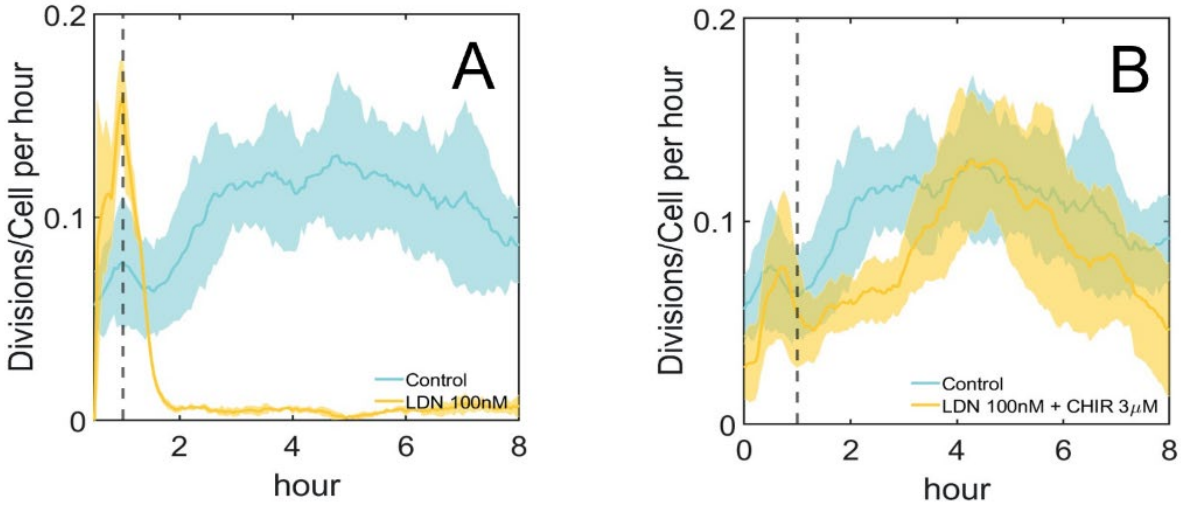

Fig. S8. CHIR rescues cell division in LDN-193189 treated embryos. (A), Cell division rate in embryos during LDN-193189 (100 nM) compared to control (not treated). (**B**), Cell division rate in embryos during LDN-193189 (100 nM) + CHIR (3 μM) compared to control (not treated). All curves show means and standard errors of division rates in at least 3 embryos

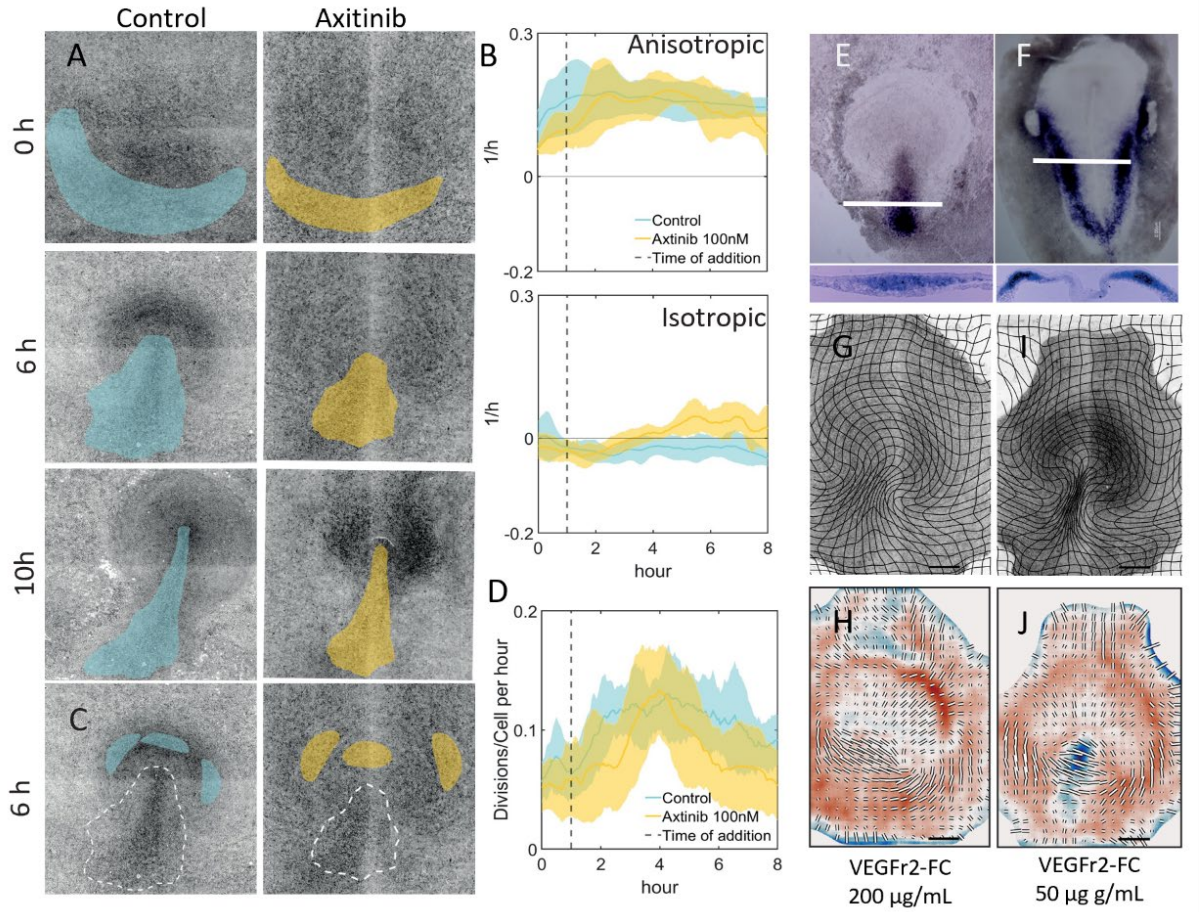

Fig. S9 Inhibition of VEGF signaling results in loss of ingression but does not inhibit intercalation. (A), Comparison of control embryo Left column and an embryo treated with the VEGF signaling inhibitor Axitinib (100nM) (right column). Images are overlaid with areas that correspond to the mesendoderm territories as determined from the dynamic morphoskeleton for the control embryo (blue) and axitinib embryo (yellow). (**B**), Strain rate tensor quantified in the blue and yellow areas in A, showing that in the control case the isotropic strain rate (upper panel) becomes negative, while in the axitinib treated embryos the isotropic component stays positive showing a lack of contraction, while the anisotropic strain component is high in both cases showing significant intercalation. The curves shown represent the mean and standard error of four or more embryos in each case. (**C, D**), Analysis of cell division rate in selected areas of the anterior epiblast of control and axitinib treated embryos. For each embryo, three analysis regions anterior to the streak (C) were followed over time and the rate of cell division (D) was calculated. The results show that axitinib treatment does not affect the rate of cell divisions. The curves in D are the average and standard errors of three regions for three embryos for each treatment. (**E, F**), In situ hybridization of the VegfR2 receptor at two stages of development (HH3 and HH5), sections show that the receptor is expressed in mesendoderm before and after ingression. (**G**): Epiblast view and deformation grid of embryo treated for 16hrs with VegfR2 Fc fragments to deplete its ligands in the light sheet microscope. (**H**), Strain rate tensor for embryo shown in H. Note the presence of intercalation of a strong anisotropic component (black bars) showing intercalation, but an absence of a negative isotropic component (blue), showing a lack of

ingression (2/2 embryos treated with VEGFr2-FC 50 µg/mL and 3/3 embryos treated with VEGFr2-FC 200 µg/mL in the light sheet microscope). (**I, J**), Lower VegfR2-Fc concentrations show a partial inhibition of streak formation. Scale bars for H, J as in Fig. S1 C.

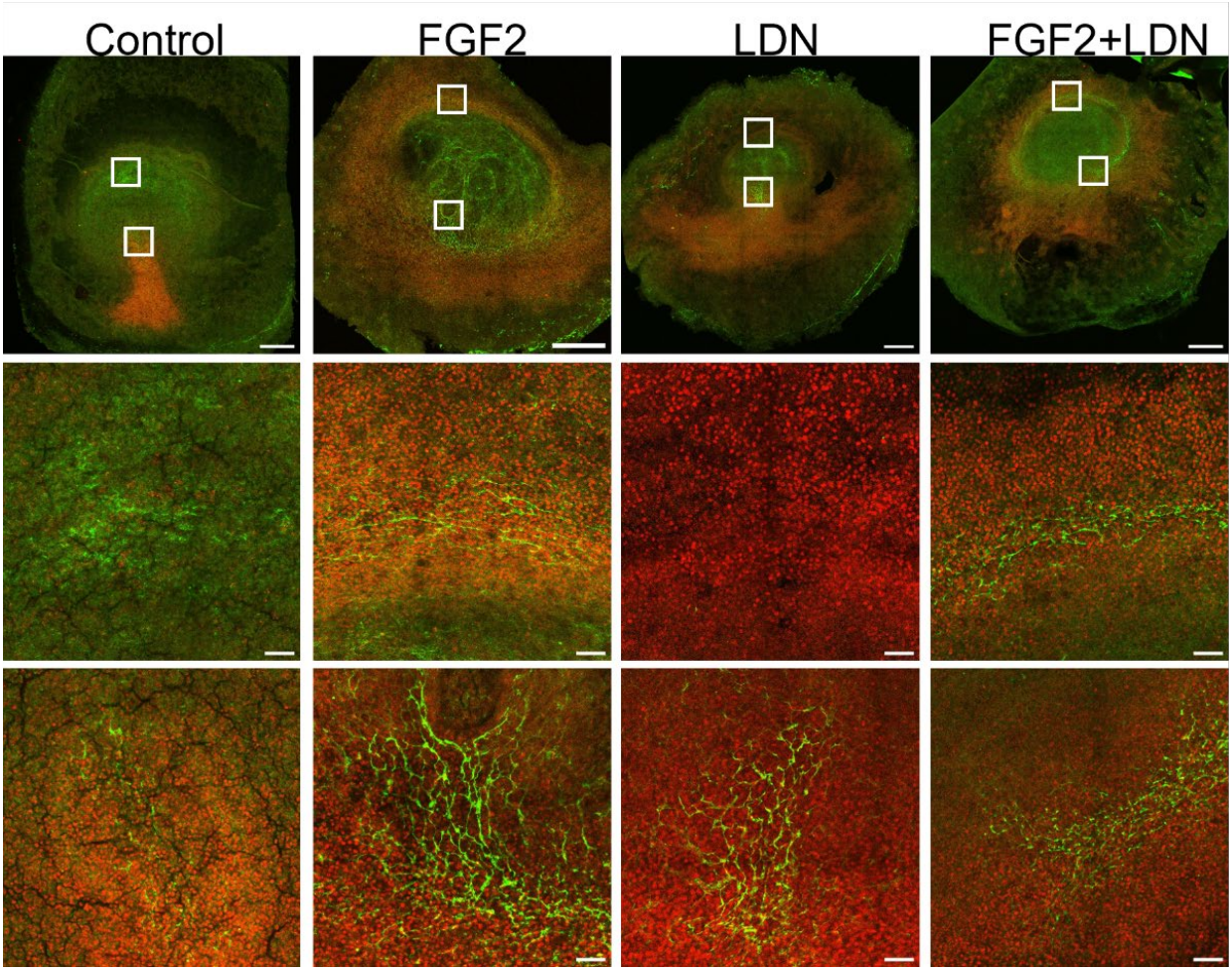

Fig. S10 Comparison of SNAI2 and TNC expression after various perturbations. Top row: Brightfield images of embryos after 16hrs in EC culture after various treatments. Second row: Confocal images of the embryos in the top row showing expression of SNAI2 (red) and TNC (green). The third and fourth rows show higher magnification images taken in front of the streak (upper white square in each image) and (lower white square in each image) at the tip of the streak. It can be seen in the control (first row) that the region anterior to the streak expresses high levels of TNC which forms a meshwork of fibrils elongated in the direction of the streak. TNC expression can also be detected in front of the streak, but it is present as a random meshwork of finer fibrils. After FGF treatment (second column) TNC expression shows the same large elongated fibrillar structure as seen in the streak of control embryos, indicating that this is also a region where cells ingress and EMT is taking place. LDN treatment TNC shows an elongated fibrillar structure in the remnant of the streak, but the anterior region shows only very low levels of TNC expression and the absence of any fibrillar network, indicating that little ingression and EMT is taking place in this region. Interestingly a combination treatment of LDN and FGF results in a clear fibrillar network indicating that EMT is taking pace and ingression will occur. The data show that the presence or absence of ingression is reflected in the FN1 network structure. Scale bars in two top rows of images are 500 μm, and scale bars in two bottom rows of images are 50 μm.

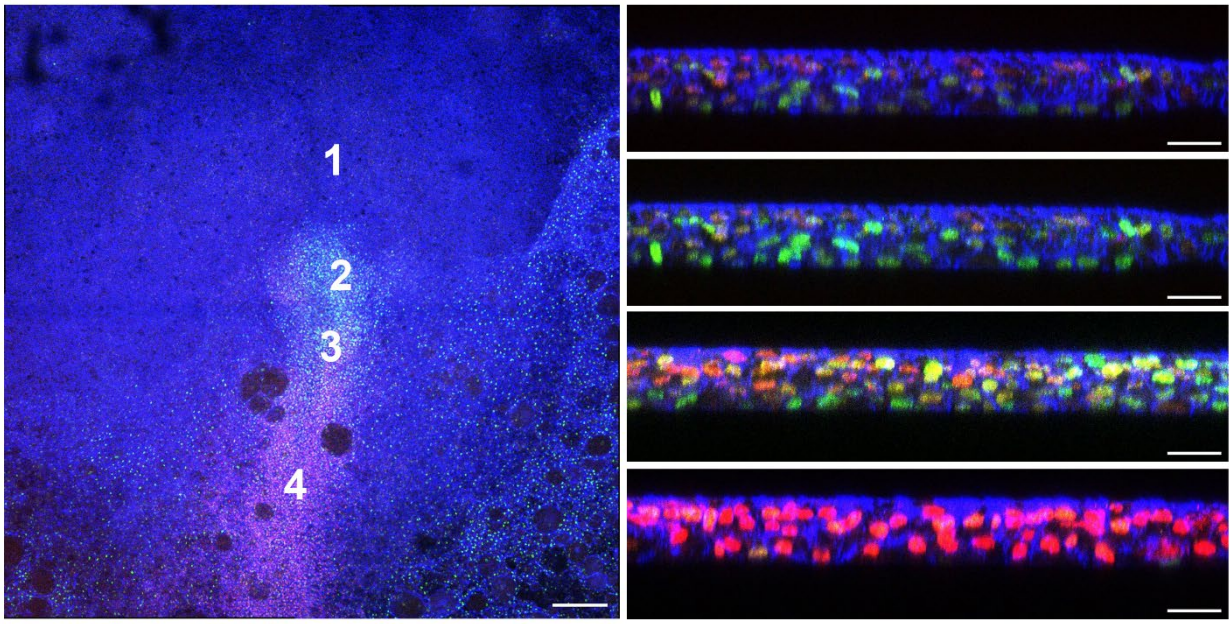

Fig. S11 Comparison of SNAI2 and HNF3B expression in various regions along the streak. (**A**), Image of streak region of HH3 embryo stained for SNAI2 (red), HNF3B (green), and actin (blue). (**B, C,D,E**), sections were taken at positions 1, 2, 3, and 4 indicated in (A).

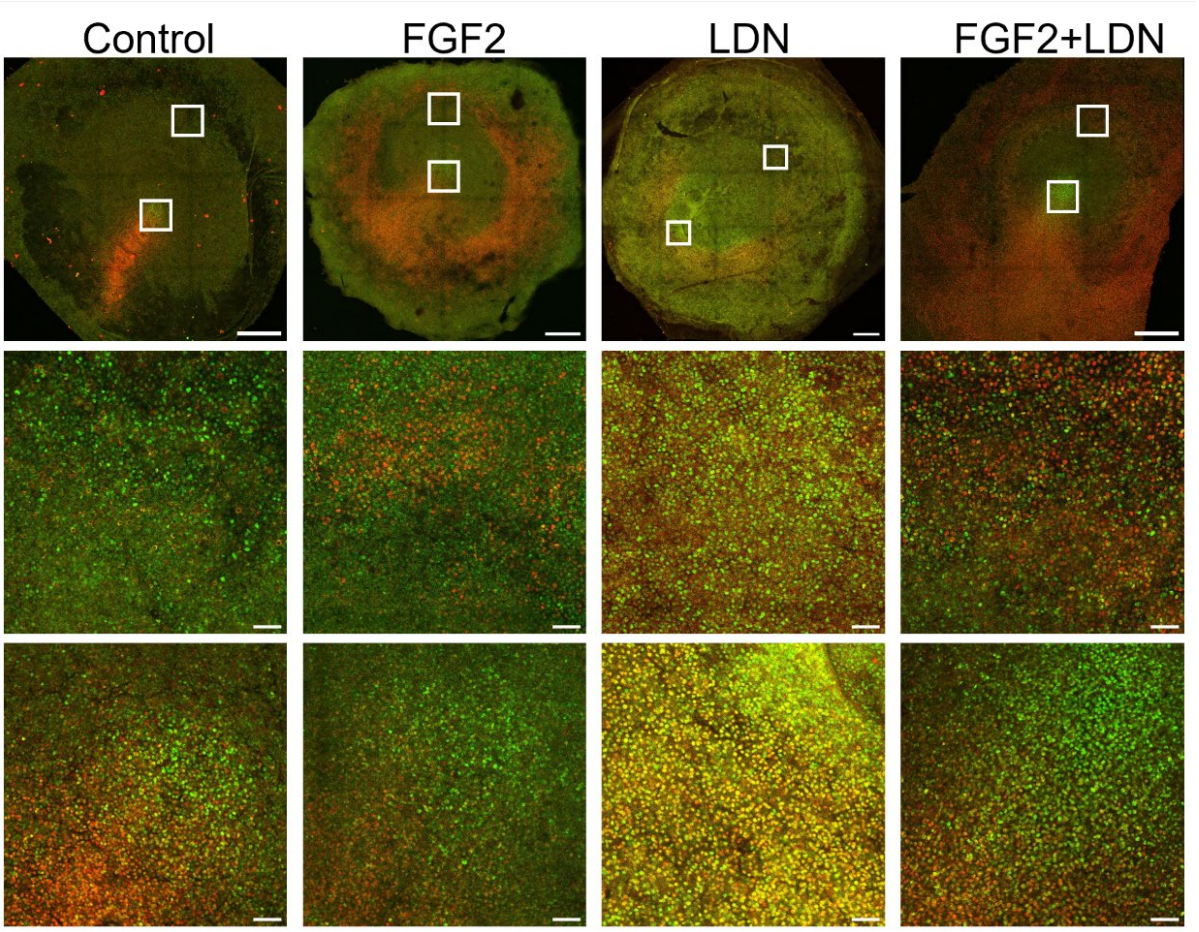

Fig. S12 Comparison of SNAI2 and HNF3B expression after various perturbations. Top row: Brightfield images of embryos after 16hrs in EC culture after various treatments. Second row: Confocal images of the embryos in the top row showing expression of SNAI2 (red) and HNF3B (green). The third and fourth rows show higher magnification images taken in front of the streak (upper white square in each image) and (lower white square in each image) at the tip of the streak. It can be seen in the control (first row) that cells in the tip of the streak are characterized by low expression of SNAI2 and high expression of HNF3B while anterior to the streak few cells express SNAI2, but some scattered cells express HNF3B. FGF treatment results in cells that express SNAI2 in a ring-shaped region at the boundary of the embryonic and extraembryonic area, mixed with cells expressing HNF3B while there is little co-expression. LDN treatment results in a decrease in the expression of SNAI2 and an increase in the expression of HNF3B in the entire epiblast, with many cells co-expressing both factors. Combined treatment of LDN and FGF results in an FGF-like phenotype with increased expression of SNAI2 and less effect on HNF3B expression. Overall, these results may indicate that FGF treatment shifts the differentiation of the cells more towards mesoderm, while LDN treatment may shift the differentiation of the cells more towards endoderm precursors. Scale bars in two top rows of images are 500 μm, and scale bars in two bottom rows of images are 50 μm.

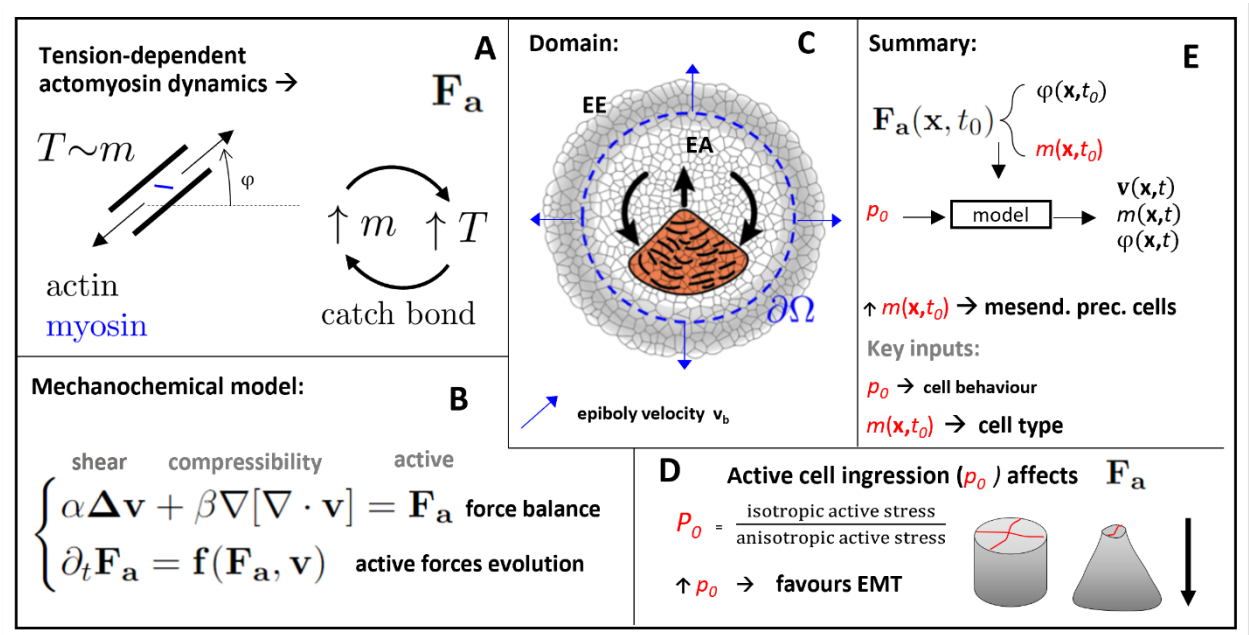

Fig. S13. **Mechanochemical model. (A),** Actomyosin cables generate active forces $\mathbf{F_a}$. $\mathbf{F_a}$ arises from spatial variation of phosphorylated myosin m and the orientation of the actomyosin cables φ. The myosin dissociation rate is tension dependent reflecting the catch-bond mechanism: cables with more myosin accumulate more myosin generating an instability that drives the flow. The φ dynamics is also coupled to the flow velocity $\boldsymbol{v}$, which transports and rotates the actomyosin cables. **(B),** The mechanochemical model consists of a force balance that includes shear forces capturing anisotropic tissue-level deformations and cell intercalations, forces induced by compressibility effects such as cell divisions, ingression and growth, and active forces $\mathbf{F_a}$. The time evolution $\mathbf{F_a}$ is coupled to the flow velocity, as summarized in A. **(C),** The domain's boundary consists of a circular boundary in the Extra-Embryonic (EE) region right outside the Embryonic Area (EA). The radial outward epiboly cell motion in the EE region enters our model as the velocity boundary condition. $\mathbf{v_b}$. **(D),** The active cell ingression (p_0) is a key nondimensional parameter in the model. p_0 is the ratio of isotropic active stress (produced by apical contraction and cell ingression) to anisotropic active stress (oriented cell intercalation). High p_0 models the ability of cells to contract isotopically, actively pulling their neighbors and inducing ingression and EMT. **(E),** Our model requires only the initial condition of $\mathbf{F_a}$, which consists of specifying $\varphi(\mathbf{x}, t_0)$ and $m(\mathbf{x}, t_0)$, and a few constant nondimensional parameters. It then provides the full spatiotemporal evolution of cell velocity, actomyosin cable orientation, and active myosin at later times. In all our model experiments, we change only two key inputs: p_0, $m(\mathbf{x},t_0)$. Decreasing p_0 models the cells' inability to undergo EMT or active cell ingression. Changes in $m(\mathbf{x},t_0)$ modulate the initial distribution of active myosin. We find that regions of high $m(\mathbf{x},t_0)$ are a good proxy for mesendoderm precursor cell type. For more details see (18).

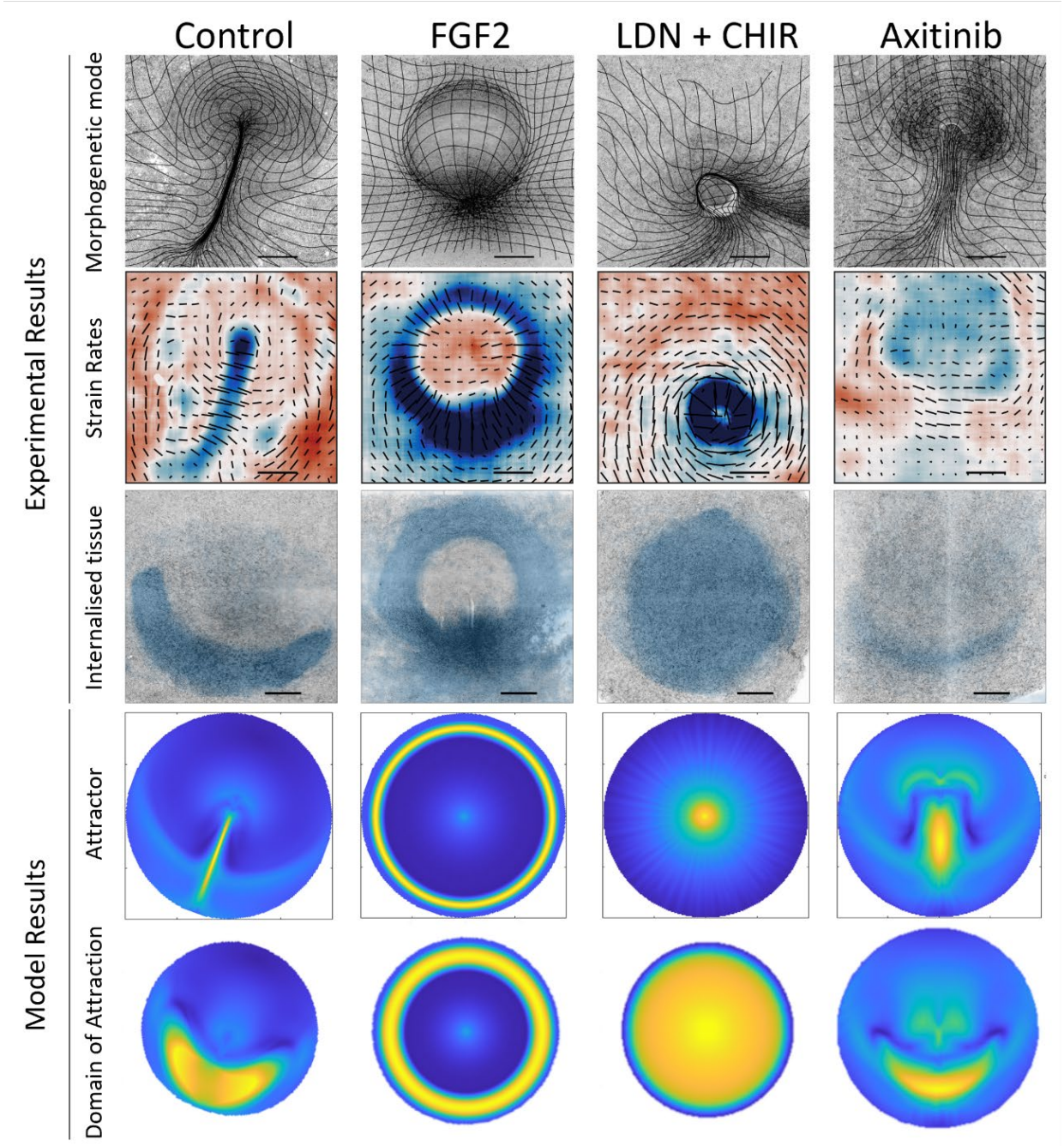

Fig. S14. Comparison of tissue dynamics measure experimentally (rows 1-3) and calculated from the mechano-chemical model (rows 4-5) after different perturbations. First row: Tissue deformation calculated from the tissue velocity field 16hrs after different perturbations as indicated in the legend. Second row: isotropic and anisotropic strain rates. Third row: domain of attraction calculated for experiments, yellow denotes the attractor. Fourth row: Lagrangian attractors. Fifth row: domain of attraction, yellow indicates tissue that will ingress during the experiment. For details of the model see (18). Data in rows 1, 2, and 3 are repetitions of data shown in Fig. 1 and Fig. 2.

Supplementary movies

Movie S1. Development of control embryo from stage HH1 to HH3+. The movie shows the development of a control embryo (left panel) and a zoom-in of the formation of the primitive streak (right panel). Inset side 650 μm. The time interval is 3 minutes.

Movie S2. Strain rates and deformation grid of control embryo from stage HH1 to HH3+. The movie shows a bright field image (top panel) and strain rate tensor of the same embryo (bottom panel) Isotropic strain rate is colored blue (contraction) to red (expansion) scale bar 500 μm. The time interval is 3 minutes.

Movie S3. Development of embryo treated with FGF signaling inhibitor LY287455. The movie shows a bright field image (top panel) and strain rate tensor of the same embryo (bottom panel). Isotropic strain rate is colored blue (contraction) to red (expansion) scale bar 500 μm. The time interval is 3 minutes.

Movie S4. Formation of an ectopic circular primitive streak in FGF2 treated embryo. The movie shows the development of an FGF2-treated embryo (left panel) and a zoom-in of the formation of the ectopic circular primitive streak (right panel). Inset side 650 μm. The time interval is 3 minutes.

Movie S5. Strain rates and deformation grid of embryo treated with FGF2. The movie shows a bright field image (top panel) and strain rate tensor of the same embryo (bottom panel) Isotropic strain rate colored blue (contraction) to red (expansion) scale bar 500 μm. The time interval is 3 minutes.

Movie S6. Migration of mesoderm cells after addition of FGF2. Focusing deeper into the embryo shows that the mesoderm cells ingressing through the circular primitive streak migrate towards the center of the embryo. The time interval is 3 minutes.

Movie S7. Formation of large invagination of the central epiblast in embryos treated with CHIR+LDN. The movie shows the development of a CHIR + LDN treated embryo (left panel) and a zoom-in of the formation of the large invagination in the central epiblast (right panel). Inset side 650 μm. The time interval is 3 minutes.

Movie S8. Strain rates and deformation grid of embryo treated with CHIR+LDN. The movie shows a bright field image (top panel) and strain rate tensor of the same embryo (bottom panel) Isotropic strain rate colored blue (contraction) to red (expansion) scale bar 500 μm. The time interval is 3 minutes.

Movie S9. Formation of an invaginating lip in an embryo treated with Axitinib. The movie shows the development of an Axitinib-treated embryo (left panel) and a zoom-in of the formation of the invaginating lip (right panel). Inset side 650 μm. The time interval is 3 minutes.

Movie S10. Strain rates and deformation grid of embryo treated with Axitinib. The movie shows a bright field image (left panel) and strain rate tensor of the same embryo (right panel) Isotropic strain rate colored blue (contraction) to red (expansion) scale bar 500 μm. The time interval is 3 minutes.

Movie S11. Comparison of the tip of streak formation in control embryo and embryo treated with 100 nM Axitinib. The time interval is 3 minutes.